JGR Space Physics

RESEARCH ARTICLE
10.1029/2019JA026848

The Variation of Resonating Magnetospheric Field Lines With Changing Geomagnetic and Solar Wind Conditions

S. J. Wharton[1], **D. M. Wright**[1], **T. K. Yeoman**[1], **M. K. James**[1], **and J. K. Sandhu**[2]

[1]Department of Physics and Astronomy, University of Leicester, Leicester, UK, [2]Mullard Space Science Laboratory, Dorking, UK

Key Points:
- Pressure pulses and Kelvin-Helmholtz instabilities excite Pc5 eigenfrequencies at $L > 5$
- Upstream waves generated in the foreshock are a source of Pc4 eigenfrequencies at $L < 4$
- Enhancements in the ring current act to decrease eigenfrequencies in the inner magnetosphere

Correspondence to:
S. J. Wharton,
sjw136@le.ac.uk

Citation:
Wharton, S. J., Wright, D. M., Yeoman, T. K., James, M. K., & Sandhu, J. K. (2019). The variation of resonating magnetospheric field lines with changing geomagnetic and solar wind conditions. *Journal of Geophysical Research: Space Physics*, *124*, 5353–5375. https://doi.org/10.1029/2019JA026848

Received 15 APR 2019
Accepted 22 JUN 2019
Accepted article online 4 JUL 2019
Published online 16 JUL 2019

Abstract Standing ultralow frequency waves redistribute energy and momentum around the Earth's magnetosphere. The eigenfrequencies of these standing waves can be measured by applying the cross-phase technique to ground magnetometer data. To make a detection, the flux tubes in the vicinity of the magnetometers must all be driven at their local eigenfrequencies by a source with a sufficient frequency width. Therefore, successful measurement of the local eigenfrequencies indicates that a broadband source is exciting the flux tubes. We have analyzed 10 years of magnetometer data with an automated cross-phase algorithm and used correlations with the OMNI data set to understand under what conditions broadband excitation occurs and how the conditions affect the eigenfrequency values. This is the largest such survey of its kind to date. We found that lower eigenfrequencies at higher latitudes ($L > 5$) and higher eigenfrequencies at lower latitudes ($L < 4$) were excited under different conditions. It was also possible to directly compare the first and third harmonics at midlatitudes. The lower eigenfrequencies were excited during more disturbed conditions, and we suggest that these harmonics are driven by solar wind pressure pulses or the Kelvin-Helmholtz instability at the magnetopause. The higher eigenfrequencies were excited when the magnetosphere was relatively quiet, and we suggest that the cause was waves generated upstream of the Earth's bow shock. The eigenfrequencies were observed to decrease in the middle magnetosphere during disturbed intervals. This is because the intensification of the ring current weakens the magnetic field. Variations in magnetic local time and latitude were also investigated.

1. Introduction

Magnetohydrodynamic (MHD) waves transport energy and momentum throughout the Earth's magnetosphere (e.g., Dungey, 1968). They can energize radiation belt particles and cause them to radially diffuse (e.g., Elkington et al., 1999) and are linked to auroral processes such as pulsating aurora (e.g., Motoba et al., 2018). These MHD waves usually have frequencies in the ultralow frequency (ULF) range, especially in the Pc3–Pc5 range as classified by Jacobs et al. (1964). These periods are from 10–600 s, or frequencies from 1.67–100 mHz. In a cold MHD plasma, these waves come in two forms: the fast mode, which propagates isotropically, and the Alfvén mode, which is field guided. In Earth's nonhomogeneous magnetosphere, the fast mode can couple to the Alfvén mode and guide energy along the field lines (Chen & Hasegawa, 1974; Southwood, 1974).

Alfvén waves partially reflect at the ionospheric footprints of the flux tube due to the high conductivity. Therefore, Alfvén waves form standing wave structures at a set of discrete frequencies called eigenfrequencies (or harmonic frequencies). The polarizations of these waves can be separated into two primary components: toroidal, where the magnetic perturbation is azimuthal, and poloidal, where that perturbation is radial (e.g., Sugiura & Wilson, 1964). Cummings et al. (1969) has shown that the polarization of the standing wave affects its frequency, especially for the fundamental mode. This is because the density of magnetic field lines is different in the radial and azimuthal directions. Hence, the eigenfrequencies of any magnetic flux tube depend upon its length, the variation of the Alfvén speed along the flux tube, and the wave polarization. The Alfvén speed is determined by the local plasma mass density and local magnetic field strength. The toroidal and poloidal mode will usually couple and produce an intermediate polarization (Elsden & Wright, 2018; Orr & Matthew, 1971; Wright & Elsden, 2016). This study focuses on standing Alfvén waves that are primarily toroidally polarized by only examining one polarization in the data.

Toroidally polarized Alfvén waves usually have a large azimuthal scale size and are thought to be excited by sources external to the magnetosphere on the dayside (e.g., Agapitov et al., 2009; James et al., 2013). These external sources generate fast mode waves at or beyond the magnetopause. These then propagate into the magnetosphere. Here they couple to flux tubes with an eigenfrequency equal to the fast mode frequency. Energy is then transferred from the fast mode into the toroidal Alfvén mode.

There are several sources of fast mode waves. First, they can be generated by the ion-cyclotron instability upstream of the Earth's bow shock (Russell et al., 1983; Troitskaya et al., 1971). This occurs when ions in the solar wind reflect off the bow shock and then resonantly interact at their gyrofrequencies with waves in the solar wind. These waves are amplified by the interaction and then convected by the super-Alfvénic solar wind through the bow shock toward the magnetopause. Foreshock transients such as magnetosheath jets can also trigger toroidal resonance (Shen et al., 2018).

The fast mode waves can also be generated directly at the magnetopause. The solar wind can contain pressure pulses that compress the magnetosphere and generate fast mode waves within the cavity (Claudepierre et al., 2010; Kepko et al., 2002). As the solar wind passes by the magnetopause, processes along the boundary can also create fast mode waves. A fast streaming solar wind can excite the Kelvin-Helmholtz instability (KHI), which creates surface waves that can then produce fast mode waves as they propagate (Pu & Kivelson, 1983). Finally, it may also be possible for the passage of flux transfer events (FTEs) to create fast mode waves as they pass across the magnetopause (Russell & Elphic, 1979). These sources can all generate fast mode waves that couple to toroidal Alfvén waves, but it is currently unclear which of these processes dominate and under what geomagnetic conditions.

To measure a field line eigenfrequency, the cross-phase technique was developed by Baransky et al. (1985) and Waters et al. (1991). This utilizes magnetometer data from two stations that are closely spaced in latitude and analyzes the phase differences between the two data sets. The frequencies where this phase difference maximizes are the eigenfrequencies. This technique requires a broadband source to excite all the flux tubes at their own eigenfrequencies such as that described by Lessard et al. (1999). This “broadband resonance” is not the same as the narrowband Field Line Resonances observed by Walker et al. (1979) Fenrich et al. (1995), or Rae et al. (2007), for example. It is described theoretically by Hasegawa et al. (1983). The ability to determine the eigenfrequencies allows us to determine the topology of the magnetosphere. Successful measurement also implies the presence of a broadband energy source. Hence, cross-phase measurements can be used as a proxy to understand this source.

Many authors have used the cross-phase technique to investigate the magnetosphere (e.g., Chi et al., 2000; Kale et al., 2007; Kawano et al., 2002; Menk et al., 1999, 2004, 2014; Obana et al., 2008; Waters et al., 1994, 1995, 1996). Of those, some have automated the process to get a continuous measurement of the eigenfrequencies (Berube et al., 2003; Chi et al., 2013; Lichtenberger et al., 2013; Sandhu, Yeoman, James, et al., 2018). The algorithm developed by Wharton et al. (2018, 2019) is more advantageous because it can detect the higher harmonics of the flux tube, whereas previous methods focused on the fundamental frequency. These harmonics have been observed in spacecraft data (e.g., Anderson et al., 1990; Engebretson et al., 1986; Takahashi & McPherron, 1982, 1984). Being able to detect multiple harmonics allows us to investigate whether different harmonics are excited by different sources or not.

In this paper, we aim to understand the conditions under which the cross-phase technique is most likely to detect the local eigenfrequency. This information can tell us when the flux tubes will resonate and can be exploited to determine which of the potential sources of toroidal ULF resonance were responsible. We have also investigated how the eigenfrequencies' values change in response to changing geomagnetic conditions. To do this, we applied the automated algorithm of Wharton et al. (2018, 2019) to observations from a network of magnetometers to create a 10-year data set of eigenfrequencies. We then compared these eigenfrequencies to the OMNI data set to understand what conditions were present when the local eigenfrequencies were detected. Never before has a data set of this size been used to investigate broadband resonance.

2. Methods

2.1. Data Sources

This study used data from the International Monitor for Auroral and Geomagnetic Effects (IMAGE) magnetometer array (Luhr, 1994). The locations of the magnetometer pairs used in this study are given in Table 1. These data have a 10-s resolution that gives a Nyquist limit of 50 mHz, high enough to cover the expected

Table 1
Locations of the Magnetometer Pairs

Magnetometers	Identity code	Midpoint geo lat.	Midpoint geo lon.	Midpoint CGM lat.	Midpoint CGM lon.	L-shell
Masi-Sørøya	MAS-SOR	68.50	22.96	66.76	106.30	6.42
Abisko-Tromsø	ABK-TRO	69.01	18.88	66.12	102.33	6.10
Ivalo-Kevo	IVA-KEV	69.16	27.15	65.71	108.91	5.91
Muonio-Masi	MUO-MAS	68.74	23.62	65.45	105.82	5.79
Kiruna-Kilpisjärvi	KIR-KIL	68.45	20.60	65.32	103.22	5.73
Sodankylä-Ivalo	SOD-IVA	67.97	26.96	64.51	107.92	5.40
Pello-Muonio	PEL-MUO	67.46	23.81	64.14	105.07	5.25
Hankasalmi-Oulujärvi	HAN-OUJ	63.39	26.92	59.84	105.34	3.96
Karmøy-Solund	KAR-SOL	60.15	5.04	57.48	85.97	3.46
Tartu-Nurmijärvi	TAR-NUR	59.38	25.56	55.68	102.54	3.15

Note. Magnetic coordinates and dipolar L-shells are based on positions in 2001 (see http://space.fmi.fi/image/www/index.php?page=stations). These values vary slightly across the time range of the study. CGM = Corrected Geomagnetic Latitude.

range of eigenfrequencies. The IMAGE array also covers a wide range of L-shells. From the stations we selected, this range is from ~3.16 to ~6.67 (when accounting for the change in magnetic latitude over the duration of the study). This allowed us to explore the latitudinal variation in eigenfrequencies.

In addition, this study used the OMNI archive to get data for the solar wind and geomagnetic indices such as the Sym H index.

2.2. Analysis Techniques

For our analysis, we used the cross-phase algorithm of Wharton et al. (2018, 2019). These papers give a full explanation, but we briefly outline it here. The algorithm uses the X-component (north-south) magnetic field data from the two stations and applies an 800-s boxcar filter. Wharton et al. (2019) modified the original algorithm to use a Lomb-Scargle (LS) cross-phase technique. This combines the LS periodogram of Lomb (1976) and Scargle (1982) with the LS phase of Hocke (1998). This means no linear interpolation is required as this technique accounts for missing data. The LS spectral technique has been used to study ULF waves by a number of authors (Bland et al., 2014; Bland & McDonald, 2016; Shi et al., 2018). The LS technique fits a range of harmonic functions with different frequencies by least squares to the data. To prevent aliasing, the highest frequency analyzed is chosen to be the Nyquist frequency (50 mHz), which is based on the time resolution of the data. The LS technique does not require us to use the same frequencies that would be used by the fast Fourier transform (FFT), but we choose the FFT grid as a starting point. We can then evenly oversample the FFT grid to increase the frequency resolution. This is because LS is a least squares procedure and not based on Fourier's theorem, so the frequency grid is not determined by the data. Bland et al. (2014) found an oversampling factor of 4 to be appropriate for studying ULF waves so we have used this value. A higher-frequency resolution means that the changes in eigenfrequency with geomagnetic conditions can be monitored with greater precision.

The remaining aspects of the algorithm are then the same as described by Wharton et al. (2018). The dynamic cross spectrum is calculated, and then smoothing and statistical tests are applied to isolate continuous and significant cross-phase minima. The algorithm then records the frequency and magnetic local times (MLTs) of each significant data point in the final cross spectrum. This set of significant eigenfrequencies forms the data set for our statistical study. This modified algorithm was applied to data from a range of station pairs, outlined in section 3.1, from January 2007 to December 2016.

It is expected that factors such as spectral window length, station separation, and longitudinal alignment will affect how often a magnetometer pair can detect its local eigenfrequency (Menk et al., 2004). However, studying these effects is outside the scope of this study. Wharton et al. (2018) found that a 40-min sliding spectral window is appropriate for identifying flux tube eigenfrequencies. With an oversampling factor of 4, this gives a frequency resolution of 0.104 mHz. This study uses the same window parameters as Wharton et al. (2018).

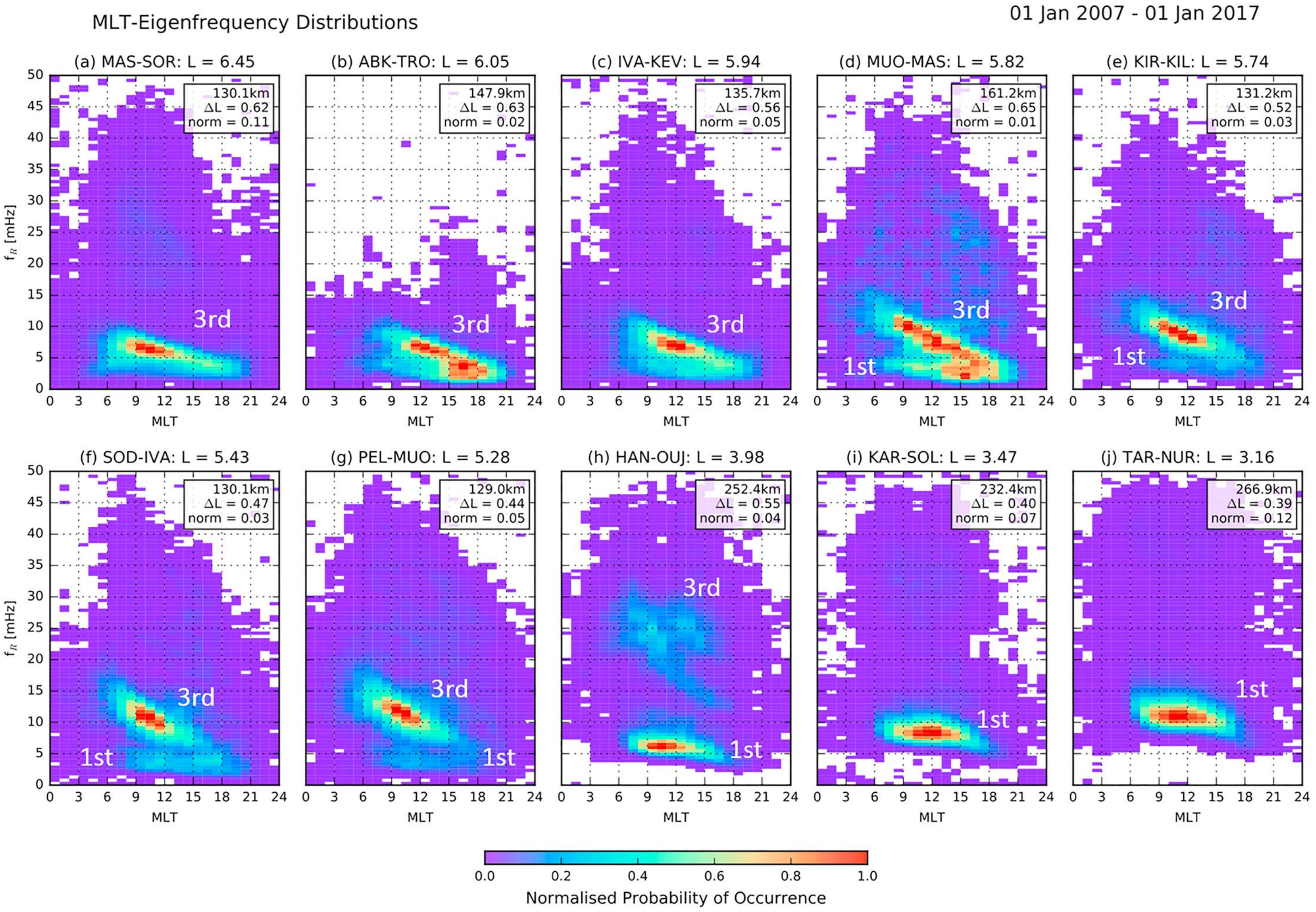

Figure 1. MLT-eigenfrequency distributions of broadband excitation occurrence for 10 International Monitor for Auroral and Geomagnetic Effects magnetometer pairs from January 2007 to January 2017. (a–e) MAS-SOR, ABK-TRO, IVA-KEV, MUO-MAS, and KIR-KIL. (f–j) SOD-IVA, PEL-MUO, HAN-OUJ, KAR-SOL, and TAR-NUR. The dipolar L-shells of the station midpoints are shown along with the pair name in the subplot titles. The color bar shows the probability of measurements in each MLT-eigenfrequency bin, normalized by the highest probability in that subplot. White spaces show empty bins. The text boxes show the separation of the magnetometer stations in both km and L-shell, and the normalizing probability density. White labels show the interpreted harmonic number of each band as explained in the text. MLT = magnetic local time.

The ionospheric conductivity will also play a significant role in determining what wave activity is present at the ground (Hughes & Southwood, 1976). Magnetometers measure the magnetic field associated with the Hall current generated in the ionosphere by the ULF wave. The Hall magnetic field has a polarization axis at 90° to the magnetic field of the ULF wave. Hence, for the toroidal mode, which has magnetic perturbations in the east-west direction above the ionosphere, we observe in the geographic X-component (north-south) in ground magnetometer data. Note that geomagnetic and geographic north are similar for the stations used here.

3. Results

3.1. Latitudinal and MLT Variations

Figure 1 shows the results of running the algorithm described in section 2.2 on 10 magnetometer pairs for 10 years of data. It presents the occurrence probability of the eigenfrequencies as a function of MLT and geomagnetic latitude. This represents a more extensive analysis than was performed in Wharton et al. (2018), which only considered data from September 2010 and from $L = 3.51$ to $L = 17.34$, or 57.7° to 76.1° geomagnetic latitude.

The names of the station pairs used and the L-shell of their latitudinal midpoint are given at the top of each subplot in Figure 1. The station pairs were chosen to achieve an optimum latitudinal separation of 110 km (Menk et al., 2004) and minimum longitudinal separation if possible. Increasing the latitudinal separation increases the phase difference between the stations (Menk et al., 1999), making cross-phase peaks more significant, but it reduces the coherency. The station pairs are organized by decreasing midpoint magnetic latitude, from Figures 1a to 1j.

In Figure 1, the color in each subplot shows the normalized probability of occurrence (henceforth referred to as probability or normalized probability as appropriate). The probability was calculated by dividing the occurrence by the maximum possible occurrence, and taking into account the bin size and data availability, allowing for data gaps. The algorithm only works for times when both stations were operating. This information can be quickly viewed at the IMAGE website (see Acknowledgements). For example, a probability of 0.06 would mean that the eigenfrequency was successfully measured at that frequency and MLT 6% of the available recording time.

The normalization was applied because some station pairs were more effective at detecting their local eigenfrequencies than others. This made comparison between pairs difficult. Normalization was carried out by dividing the probability values in each subplot by the maximum probability value in that subplot. This value, *norm*, is given in the text box. The norm value is a proxy for how effective that station pair was at measuring its local eigenfrequency. Also included in the text boxes are the separation of the stations in that pair in both kilometers and L-shell. White spaces show MLT-eigenfrequency bins that had no measurements in them.

A band of high normalized probability (red) is centered at ~7 mHz in Figure 1a. In Figure 1g (which is at a lower latitude), this band had increased to ~12 mHz. In Figure 1d, another band appeared at ~3 mHz, which was also observed in Figures 1e–1j. In Figures 1a–1g, the higher-frequency band was more commonly observed. However, in Figures 1h–1j, the normalized probability of the upper band decreased with latitude and the band increased in frequency until it was unobservable in Figure 1i. The lower-frequency band then had a greater normalized probability, and its frequency increased up to ~11 mHz in Figure 1j. These features are discussed further in section 4.1.

Most observations in Figure 1 occurred between ~4 and ~20 mHz and occurred mostly in the dayside. There was also variation in MLT for both eigenfrequency and occurrence probability. The eigenfrequencies were higher in the morning hours relative to the afternoon at all latitudes, especially for the higher-frequency band. The probability maximized in the prenoon sector for all latitudes. Howard and Menk (2005) and Takahashi et al. (2016) have noted that toroidal waves are preferentially excited in the morning sector, which agrees with this observation.

Previous work suggests that the eigenfrequency gradient with latitude will reverse across a sufficiently sharp plasmapause (e.g.,Menk et al., 2004). This would result in the eigenfrequency being lower just inside the plasmasphere compared to the plasmatrough outside. On average, the plasmapause exists between $L = 4$ and $L = 5$ (O'Brien & Moldwin, 2003). Unfortunately, this region is not well covered by the magnetometer pairs. Data from Figures 1g and 1h likely came from magnetometer pairs that straddled the plasmapause, and there was a clear difference between the two panels. In Figure 1g, the higher-frequency band had a greater probability than the lower band, whereas in Figure 1h, it was the lower-frequency band that was more commonly seen. However, the lower-frequency band still increased in eigenfrequency when moving to the lower latitude. In other words, there was no reduction in eigenfrequency observed when traversing the plasmapause region.

Analysis on the Pello-Muonio pair (Figure 1g) by Wharton et al. (2018) confirmed that the rarer, lower-frequency band was the fundamental and that the more commonly occurring band was the third harmonic. These harmonic numbers have been added to the bands in Figure 1. This conclusion was drawn after investigating the frequency spacing between the harmonics and looking at the shape of the plasma mass density distributions calculated with and without the assumption that the second harmonic was missing. The third harmonic is also the most frequently observed harmonic in spacecraft data at $L > 4$ (e.g., Anderson et al., 1990; Engebretson et al., 1986; Takahashi & McPherron, 1982, Takahashi & Denton, 2007; Takahashi et al., 2010). It is not possible to know with 100% certainty that these are the correct harmonic numbers without knowing the field-aligned structure of the waves, but we use this assumption for the harmonic numbers throughout this paper.

It should be stated that just because the third harmonic was more frequently observed does not mean it contains more power than the fundamental. Results in Wharton et al. (2018) found that measurements of the fundamental had a greater corresponding power than those in the more regularly observed third harmonic. This interpretation also means that the second harmonic was missing, which has been noted by other authors (e.g., Lanzerotti & Fukunishi, 1974, Wharton et al., 2018). This is because the field-aligned structure of the driver is usually symmetric about the magnetic equator (Claudepierre et al., 2010). In such circumstances, the second harmonic is not driven because it has an electric field node at the equator. However, the even harmonics are observed in spacecraft data (e.g., Engebretson et al., 1986), so it is unclear why they are not observed on the ground.

The rest of this paper focusses on the data from the Masi-Sørøya, Pello-Muonio, and Tartu-Nurmijärvi station pairs. These pairs were chosen because they had the greatest norm values and covered the full range of magnetic latitude. Particular attention was paid to the Pello-Muonio pair because it was analyzed in detail in Wharton et al. (2018). Therefore, we are confident the observations were of the fundamental and third harmonic. Using observations of both harmonics allowed us to compare high- and low-frequency excitation.

3.2. Variations With Geomagnetic Conditions

In this section, we investigate how different geomagnetic conditions affected the detection of the eigenfrequencies for the three magnetometer pairs noted at the end of section section 3.1. For this, we used the OMNI data set with a 5-min time resolution to match the time increment of the dynamic spectra used to calculate the cross-phase spectra (Wharton et al., 2018). We have binned the results of the algorithm by a range of solar wind and geomagnetic parameters. These comparisons can be used to identify under what conditions the flux tubes will resonate and a detection will be made.

In order to account for the time delay between a change in a given solar wind property, represented by an OMNI parameter, and that change impacting the structure of the magnetosphere, we took the OMNI data value and calculated the mean of the previous hour's data. We then compared the algorithm data with this "previous hour mean" data. This helped to remove the effects that any short-lived "spikes" in the data may have had on the correlations.

We investigated changes with the following variables: solar wind velocity v, solar wind density n, solar wind dynamic pressure P, the modulus of the solar wind dynamic spatial pressure gradient $|\nabla P|$, Sym H index, interplanetary magnetic field (IMF) Bz component Bz, IMF magnitude B, and IMF cone angle θ_c. Of these eight parameters, $|\nabla P|$, B, and θ_c were calculated from other parameters in the OMNI data set. Throughout the rest of this paper, the term solar wind parameters/variables includes the Sym H index for convenience.

As the dynamic pressure largely determines the position of the magnetopause, so the spatial gradient in the dynamic pressure determines the rate at which the magnetopause moves inwards or outwards. It is through the motion of the magnetopause by pressure changes that energy can be transferred via fast mode waves into the magnetosphere. If there is a strong spatial gradient in pressure, this will cause the magnetopause to accelerate inwards or outwards, which will generate fast mode waves that can propagate through the magnetosphere. By comparing to this variable, we can assess whether the pressure pulse mechanism is important in exciting the flux tubes.

The spatial pressure gradient, ∇P, was calculated using equation (1). $\frac{\mathrm{d}P}{\mathrm{d}t}$ is the time derivative of P. $\frac{\mathrm{d}P}{\mathrm{d}t}$ was calculated for each data point by taking a box five data points wide, or 25 min, centered on the data point in question. Increasing the size of this box served to smooth out the pressure gradient, but it was decided that this size was an acceptable compromise between removing "spikes" in the data and smoothing over the gradients. A straight line was then fitted to these five data points to get the gradient $\frac{\mathrm{d}P}{\mathrm{d}t}$. Then ∇P could then be calculated. This was repeated for every data point in the dynamic pressure time series.

$$\nabla P = \frac{1}{v}\frac{\mathrm{d}P}{\mathrm{d}t} \tag{1}$$

θ_c was calculated using equation (2).

$$\theta_c = \arccos\left(\frac{|B_x|}{B}\right) \tag{2}$$

We also looked at relationships with other OMNI parameters, those being IMF B_y and B_x components, temperature, IMF electric field, IMF clock and spiral angles, Alfvén Mach number, and the magnetospheric

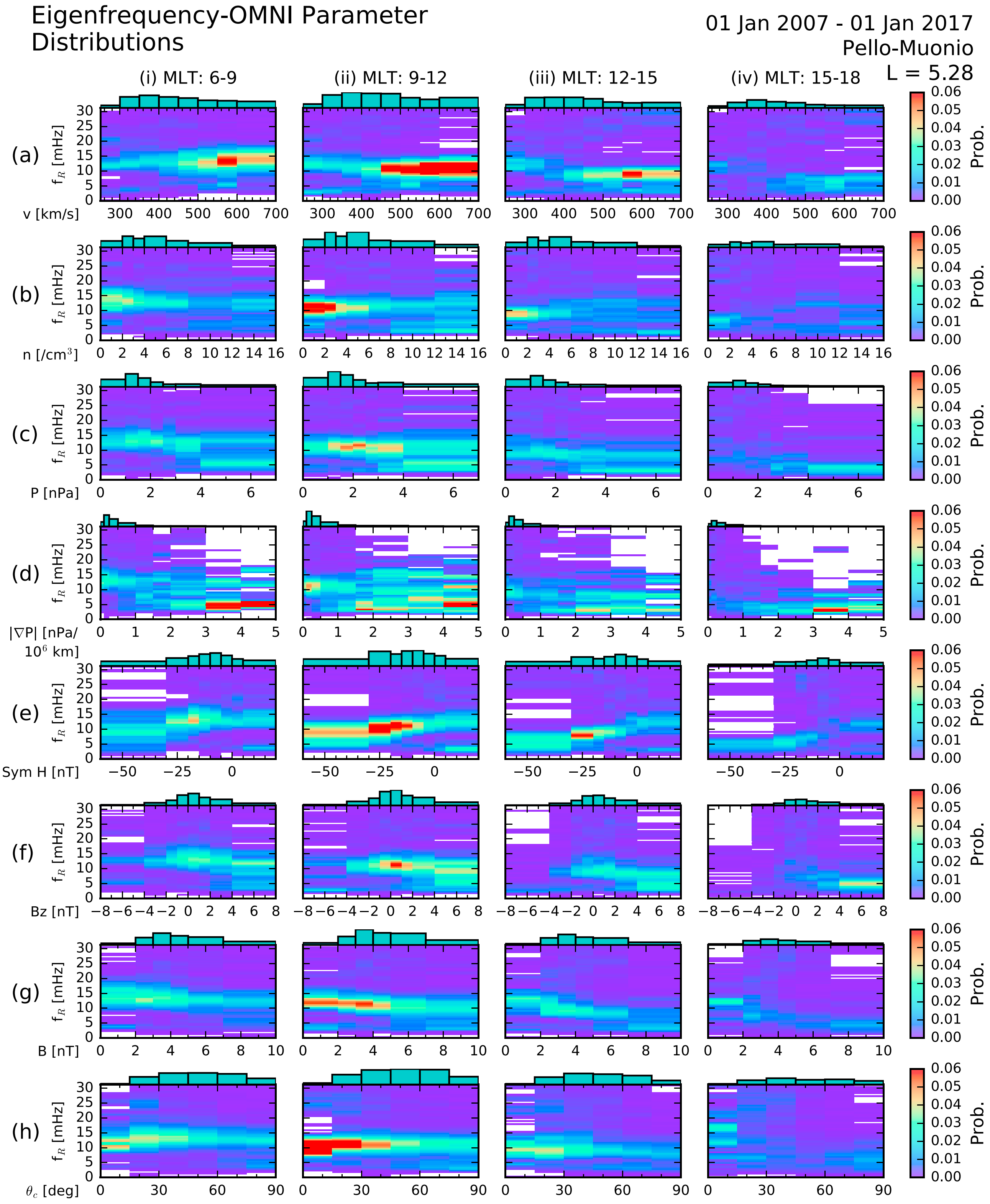

Figure 2. Eigenfrequency-OMNI parameter distributions for eight OMNI parameters using the PEL-MUO station pair. (a) Solar wind velocity v, (b) solar wind density n, (c) solar wind dynamic pressure P, (d) modulus of the solar wind dynamic pressure gradient $|\nabla P|$, (e) Sym H index, (f) IMF B_z component , (g) IMF magnitude B, and (h) IMF cone angle θ_c. The four columns, (i) to (iv), represent four MLT bins, which are written at the top. Color in the main plot represents probability (see color bars on right). The bar plot above each colored plot shows the amount of data in each OMNI parameter column. IMF = interplanetary magnetic field; MLT = magnetic local time.

coupling function defined by Milan et al. (2012). None of these parameters added any new information to the picture presented in the following subsections that we could see. Hence, they have been omitted from this manuscript.

3.2.1. Midlatitudes

First, we looked at the Pello-Muonio station pair because this was the pair studied in most detail previously by Wharton et al. (2018). Figure 2 shows the Pello-Muonio broadband excitation probability dataset binned by the eight parameters from (or derived from) the OMNI data set detailed above, corresponding to the rows in Figure 2. Each column represents a dayside MLT sector 3-hr wide (see top of each column).

The subplots consist of an eigenfrequency-OMNI parameter distribution and a bar plot at the top. The distribution was constructed by taking the Pello-Muonio data (in that MLT sector) and dividing the data into several bins of an OMNI parameter. The bar plot shows how much data are in each OMNI parameter bin. This bar plot was used to even out the number of data points in each OMNI bin by changing the width of the bins. As this was the bar plot's only purpose, its scale has not been shown to save space. A typical, large column might contain ~100,000 data points as represented by the bar's height, not area. The bar's width matches the width of the OMNI bin. The color in the eigenfrequency-OMNI distribution represents the probability of occurrence, which has been weighted by the fraction of time spent in each OMNI parameter bin. This format was used to see under what conditions the flux tubes are excited. We now describe each parameter in turn.

Figure 2a shows that for all MLT sectors, the probability increased with solar wind velocity. This agrees with observations by Russell et al. (1983). This was the case for the third harmonic, but it was less clear for the fundamental which is more difficult to see. There is also an interesting difference in how the eigenfrequency of the third harmonic changed between different MLT sectors. The eigenfrequency appeared to increase with velocity in Figure 2a-i but decrease in Figures 2a-ii to 2a-iv. As it is difficult to tell whether there are significant gradients in the eigenfrequencies by eye, the eigenfrequency gradients have been investigated in more detail in section 4.3.

Unlike the dependence on solar wind velocity, the probability decreased with increasing solar wind density for the third harmonic, as seen in Figure 2b. This is most likely because the solar wind density and velocity are anticorrelated (e.g.,Neugebauer & Snyder, 1966). However, the fundamental showed different behavior and actually became more likely when the solar wind was denser. This is most clear in Figure 2b-ii.

The dynamic pressure determines the size of the magnetopause and affects the magnetic field structure and plasma content of the magnetosphere. Therefore, we binned the Pello-Muonio data set by dynamic pressure regardless of its dependence on solar wind velocity and density. Figure 2c illustrates how the probability of detection changed with dynamic pressure. The probability did not change as significantly as with solar wind velocity and density as it did with increasing dynamic pressure. This is because the inverse dependencies on velocity and density were canceling each other out. We can see an interesting difference between the fundamental and third harmonics though. The third harmonic was more prevalent at lower pressures and the fundamental more at higher pressures. The fundamental also had a wider spread in MLT (see Figure 2c-iv). There was arguably a slight decrease in the eigenfrequency of the third harmonic with increasing pressure too.

Figure 2d presents the result of binning the Pello-Muonio data by the modulus of the spatial pressure gradient. This data set contained a lot of variability. Experimentation with the boundaries of the spatial pressure gradient found that there was no difference in the results for a positive or negative gradient, so we have displayed its modulus to increase the amount of data in the bins. The third harmonic was most likely to be detected for lower-pressure gradients, when the magnetopause was relatively still. However, the fundamental was more likely for higher-pressure gradients when the magnetopause was being compressed. The fundamental also had a wider spread in MLT (Figure 2d-iv).

Next, we looked at the impact of the ring current on the occurrence probability and the eigenfrequencies. The Sym H index had the most notable eigenfrequency variation. Figure 2e shows the eigenfrequency increased with increasing Sym H index, as the magnetosphere became quieter. The probability of occurrence was greatest near −25 nT, not at the most disturbed times. It is difficult to separate the fundamental and third harmonic in this data, making interpretation more difficult.

Figure 2f shows the Pello-Muonio data binned by IMF Bz component. We can see that the third harmonic was present for both weak northward and weak southward IMF. However, the fundamental frequency was only observed under strong northward IMF. From Figure 2f-iv, we can see that the fundamental was excited toward dusk, whereas the third harmonic was not.

Figure 2g demonstrates that the eigenfrequency of the third harmonic decreased with increasing IMF strength. This reduction in frequency was also observed by Takahashi et al. (1984). The harmonic was also more likely to be excited for a weaker IMF. The effect on the fundamental is not so clear in Figure 2g.

Finally, Figure 2h shows the Pello-Muonio data set binned by IMF cone angle. The probability of making a detection of the third harmonic was more likely when the IMF cone angle was below 30°. Both Russell et al. (1983) and Takahashi et al. (1984) have observed this relationship with cone angle. Figure 2 also shows an enhancement in probability at high cone angles for the fundamental frequency in the 9–12 MLT sector.

3.2.2. Higher Latitudes

In order to better understand the relationships between OMNI parameters and probability in section 3.2.1, we investigated whether these relationships existed at other latitudes. First, we examined the Masi-Sørøya pair, which is at a higher latitude than the Pello-Muonio pair. Figure 3 shows data from the Masi-Sørøya station pair in an equivalent format to Figure 2. Based on the arguments from section 3.1, we assumed that the strong band of probability seen in subplots of Figure 3 was the third harmonic. Note that the probability scale in Figure 3 is different to that in Figure 2.

We now discuss the observations for the Masi-Sørøya data set relative to those from the Pello-Muonio data set. First, we can see that the solar wind velocity and density followed the same relationship at Masi-Sørøya as for at Pello-Muonio. However, the probability increased more strongly with solar wind dynamic pressure at Pello-Muonio. The relationship between probability and the modulus of the spatial pressure gradient was also unclear, though it was much less variable than for the Pello-Muonio pair.

The relationship between probability and Sym H index at Masi-Sørøya was stronger than for Pello-Muonio. There was an increase in eigenfrequency as the Sym H index increased and the probability was greater for lower Sym H.

The relationship between probability and IMF Bz component is similar to the Pello-Muonio station pair. The probability increased for northward IMF. For the IMF magnitude, the probability was highest for values of B that were higher than at the Pello-Muonio pair. However, the eigenfrequency still decreased as the IMF magnitude became stronger. Finally, there was the same dependence with cone angle, where the probability maximized for smaller cone angles.

3.2.3. Lower Latitudes

We then looked at equivalent data for a lower latitude. Figure 4 shows data from the Tartu-Nurmijärvi station pair in the same format as Figures 2 and 3. This pair is expected to predominantly reside within the plasmasphere. The band of high probability in Figure 4 was the fundamental frequency, based on arguments in section 3.1.

The relationship between probability and velocity is different than in Figures 2 and 3. Instead of the probability maximizing for higher solar wind velocities, it instead was highest at an average solar wind velocity. The eigenfrequency also increased with the solar wind velocity. This alternative relationship was also reflected in the density, which showed that the solar wind density made little difference to the probability of detection. The eigenfrequency also decreased with density. The relationship between probability and solar wind dynamic pressure was also different. The probability was stronger for weaker pressures. With regards to the spatial pressure gradient, the relationship was less clear, though it may be that the eigenfrequency tended to increase for a stronger gradient.

The largest difference with respect to the higher latitudes was due to the Sym H index. The probability was higher and the eigenfrequency was lowest for high Sym H indices. This is the opposite case to that at higher latitudes.

The relationship between probability and B_z was consistent at all latitudes, with a higher probability of occurrence during northward IMF. Correlating the probability with IMF magnitude showed that the probability maximized for low IMF magnitudes. This forms a consistent pattern between the three latitudes, with the probability maximizing at increasingly high values of IMF magnitude as the latitude increases. Finally, the dependencies of probability and eigenfrequency on cone angle were the same for the low latitudes.

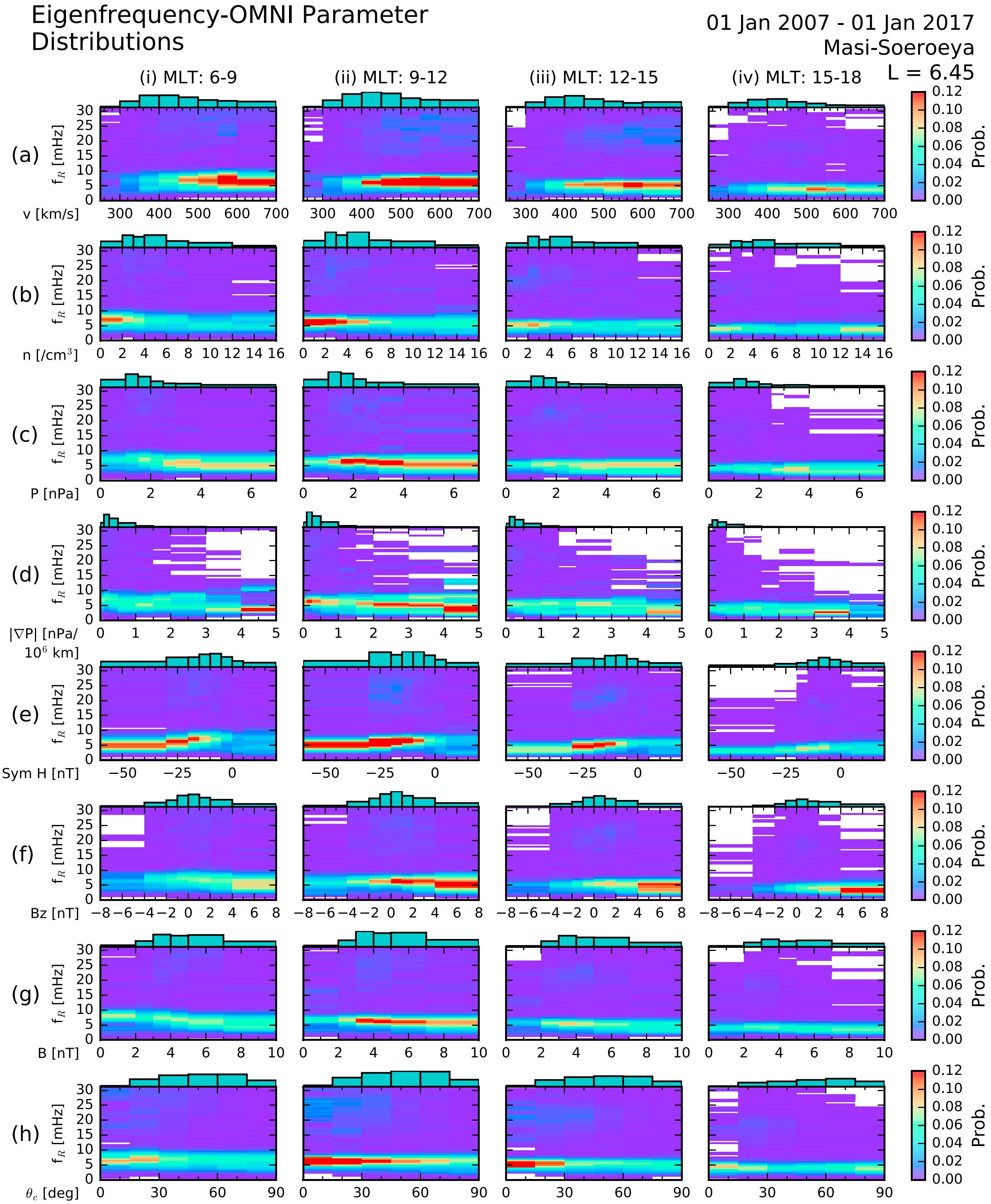

Figure 3. Eigenfrequency-OMNI parameter distributions for eight OMNI parameters using the MAS-SOR station pair. (a) Solar wind velocity, (b) solar wind density, (c) solar wind dynamic pressure, (d) modulus of the solar wind dynamic pressure gradient, (e) Sym H index, (f) IMF B_z component, (g) IMF magnitude, and (h) IMF cone angle. The four columns, (i) to (iv), represent four MLT bins, which are written at the top. Color in the main plot represents probability (see color bars on right). The bar plot above each colored plot shows the amount of data in each OMNI parameter column. IMF = interplanetary magnetic field; MLT = magnetic local time.

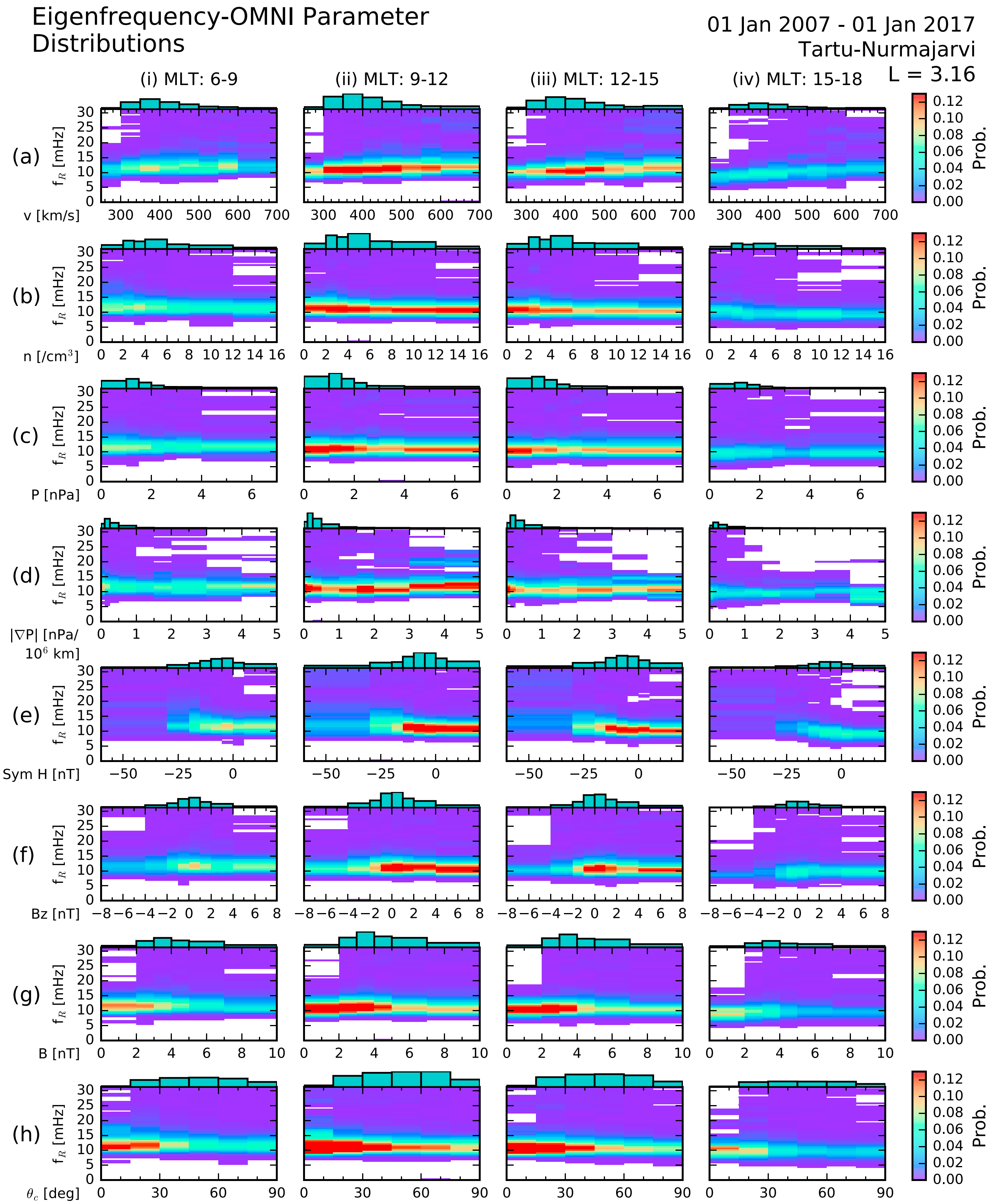

Figure 4. Eigenfrequency-OMNI parameter distributions for eight OMNI parameters using the TAR-NUR station pair. (a) Solar wind velocity, (b) solar wind density, (c) solar wind dynamic pressure, (d) modulus of the solar wind dynamic pressure gradient, (e) Sym H index, (f) IMF B_z component, (g) IMF magnitude, and (h) IMF cone angle. The four columns, (i) to (iv), represent four MLT bins, which are written at the top. Color in the main plot represents probability (see color bars on right). The bar plot above each colored plot shows the amount of data in each OMNI parameter column. IMF = interplanetary magnetic field; MLT = magnetic local time.

4. Discussion

4.1. Variations With Geomagnetic Latitude and MLT

In section 3.1, Figure 1 showed that the probability of detection of the broadband excitation of flux tubes and the values of the eigenfrequencies themselves changed for different latitudes and local times. We review expectations based on previous work before discussing our results.

It has commonly been found that eigenfrequencies decrease with increasing magnetic latitude (e.g., Baransky et al., 1989; Clausen et al., 2008; Samson et al., 1971; Wharton et al., 2018). This has been attributed to the lengthening of the field lines toward the magnetic poles. However, a reversal in this trend has been observed at a sufficiently sharp plasmapause. This is thought to be because of the sharp increase in plasma mass density on the equatorward side (e.g., Kale et al., 2007; Orr & Hanson, 1981; Menk et al., 1999, 2004 Milling et al., 2001). An increase in plasma mass density inside the plasmapause can reduce the Alfvén velocity sufficiently to reverse the trend in eigenfrequency with latitude. At very low latitudes ($L < 1.5$; outside of the range of this study), the eigenfrequencies have been observed to decrease again (Kawano et al., 2002). This is believed to be because of mass loading of flux tubes near the equator by heavy ionospheric ions.

One observation from Figure 1 is that some station pairs observed their local eigenfrequencies more often than others. This difference in detection rate could be due to station separation (see text boxes in each subplot of Figure 1) or factors affecting the magnetometer, such as ground induction effects. However, there was no correlation between the norm value and station separation. Potentially, flux tubes could statistically be excited at some magnetic latitudes more than others but this seems unlikely as there is no discernable pattern with magnetic latitude. Hence, we think this variation in detection between magnetometer pairs is related to their geographical locations, where the local geology could affect magnetic field measurements, and the sensitivity of the instruments. An in depth study would be needed to fully understand these effects.

Figure 1 demonstrated that most eigenfrequencies existed between ~4 and ~16 mHz, regardless of the harmonic identified. This raises the interesting possibility that the main drivers of these waves have a preferred frequency range, exciting the third harmonic at high latitudes and the fundamental at low latitudes. Another possibility is that the harmonics above ~16 mHz were excited but their scale size was smaller so the perturbations were not seen at the ground due to the spatial integration effect of the ionosphere (Hughes & Southwood, 1976).

Another observation from Figure 1 was that the measurements almost exclusively appeared on the dayside. This could be because the Hall conductivity at night is too low to generate a detectable magnetic field. Much of the wave activity on the nightside is driven by substorms too, which drive poloidal mode waves (e.g., James et al., 2013; Wright & Yeoman T. K., 1999; Yeoman et al., 2010;). However, all of these observations were of the toroidal mode. The sources of these toroidal waves are all thought to exist in the dayside which would explain this observation (see section 1).

Figure 1 showed there was a variation in both frequency and normalized probability with MLT. The eigenfrequency of the third harmonic decreased with MLT in Figures 1a–1h. The fundamental exhibited a shallower decrease in eigenfrequency with MLT in Figures 1h–1j. One might expect the eigenfrequency to be greatest at noon, where the magnetic field lines are shortest and the magnetic field strength strongest. However, the plasma mass density is higher in the afternoon sector than the morning because the flux tubes refill with plasma throughout the day. This causes the eigenfrequencies to decrease (Chappell et al., 1971; Chi et al., 2013; Mathie et al., 1999; Poulter et al., 1984; Sandhu, Yeoman, James, et al., 2018; Takahashi & McPherron, 1982; Warner & Orr, 1979; Wharton et al., 2018). The heavy ion concentration has also been observed to increase in the afternoon sector (Sandhu et al., 2016a, 2016b).

A clear bias for detection in the morning sector compared to the afternoon was also seen in Figure 1. Specifically, the probability of detection was a maximum in the hours before noon at all latitudes. Many other authors have also observed this asymmetry for toroidal Pc5 waves in spacecraft data (e.g., Howard & Menk, 2005; Takahashi et al., 2016). Takahashi et al. (2016) found that this asymmetry existed regardless of the orientation of the Parker spiral and ruled out the KHI as a cause of this asymmetry. Instead, they stated that the source of the asymmetry must be internal to the magnetosphere. Wright et al. (2018) showed using simulations how an asymmetric plasma distribution can refract fast mode waves. This created an azimuthal magnetic pressure asymmetry which resulted in more flux tube excitation in the morning than the afternoon. The asymmetric plasma mass density distribution is also the cause of the lower eigenfrequencies

Table 2
Summary of Observations From Section 3

OMNI parameter	Higher latitude (MAS-SOR)	Middle latitude (PEL-MUO)	Lower latitude (TAR-NUR)
v	Pr. increases with v	Pr. increases with v f_R decreases with v at 15–18 MLT	Pr. maximizes for mean v
n	Pr. decreases with n	Pr. decreases with n Pr. maximizes for mean P (third)	Pr. indep. of n
P	Pr. increase with P	Pr. increases with P (first) f_R decreases with P at 9–15 MLT	Pr. decreases with P
$\lvert\nabla P\rvert$	Pr. increases with $\lvert\nabla P\rvert$ f_R decreases with $\lvert\nabla P\rvert$ at 6–9 MLT	Pr. maximizes for small $\lvert\nabla P\rvert$ (third) Pr. maximizes for large $\lvert\nabla P\rvert$ (first) f_R decreases with $\lvert\nabla P\rvert$ at 6–15 MLT	
Sym H	Pr. decreases with Sym H	Pr. maximizes for mean Sym H f_R increases with Sym H at 12–18 MLT	Pr. increase with Sym H
B_z	Pr. increases with B_z	Pr. maximizes near $B_z = 0$ (third) Pr. increases with B_z (first) f_R decreases with $\lvert B_z\rvert$ at 15–18 MLT	Pr. increases with B_z
B	Pr. maximizes for higher B	Pr. maximizes for lower B f_R decreases with B at 12-18 MLT	Pr. maximizes for lower B
θ_c	Pr. decreases with θ_c	Pr. decreases with θ_c	Pr. decreases with θ_c

Note. Detailed are the changes in probability (Pr.) with respective parameters and significant eigenfrequency variations, as determined in section 4.3. MLT = magnetic local time.

in the afternoon sector. However, Henry et al. (2017) found that the KHI was statistically more common on the dawnside which could also account for this asymmetry. However, our discussion in the following sections establishes that both the KHI and pressure pulse mechanism could be drivers of the fundamental eigenmode. If KHI is the dominant driver, then this is likely to be the source of the asymmetry, whereas if the pressure pulse mechanism is the dominant source, then this supports the hypothesis of Wright et al. (2018) because this source is symmetric in MLT. Therefore, the asymmetry would be internal to the magnetosphere.

Finally, Figure 1 showed that there was not a sharp decrease in eigenfrequency when crossing the expected position of the plasmapause. However, a sharp decrease in frequency might not be expected because these measurements were averages over 10 years so any sudden changes in eigenfrequency will have been smoothed over. The magnetometers are also integrating over a wide area of the ionosphere (Hughes & Southwood, 1976) so the plasmapause will have appeared blurred from the ground. The plasmapause also varies in location and the sharpness of the boundary changes with time (e.g., Dent et al., 2006). This will contribute to smoothing out the boundary in the statistical analysis.

4.2. Variation in Occurrence With Solar Wind Properties

Table 2 summarizes the key observations from the data in section 3. This table can be used to understand the conditions that were present when measurements of broadband resonance were made at high and low latitudes. The table contains observations, in a qualitative manner, for when the probability of detection was highest with respect to a solar wind variable. The table also details significant relationships between the eigenfrequency and a solar wind parameter. The method by which these are determined is explained in section 4.3 along with a relevant discussion.

For high latitudes, higher occurrence probabilities were seen for a fast, low-density solar wind with a high dynamic pressure. Higher probability was observed for higher-pressure gradients and more negative Sym H indices. Finally, the IMF component was usually northward and the cone angle was often less than 30°. These criteria suggest that resonant activity at high latitudes was more likely during disturbed conditions.

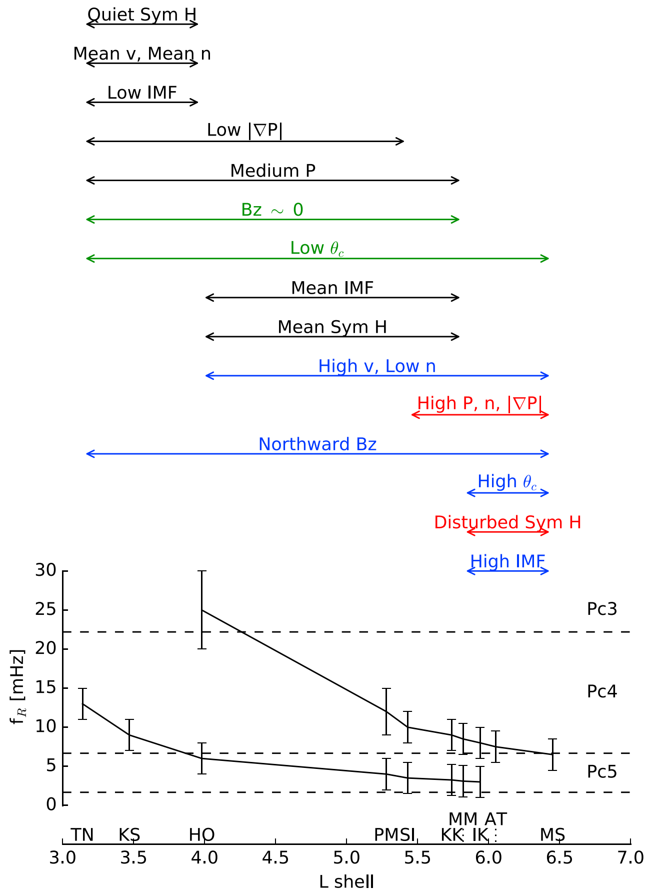

Figure 5. Diagram to qualitatively organize the observations with magnetic L-shell. Bottom: The station pairs are written as two letters on the *x* axis. TN = Tartu-Nurmijärvi. KS = Karmoey-Solund. HO = Hankasalmi-Oulujarvi. PM = Pello-Muonio. SI = Sodankyla-Ivalo. KK = Kiruna-Kilpijarvi. MM = Muono-Masi. IK = Ivalo-Kevo. AT = Abisko-Tromso. MS = Masi-Sørøya. Middle: The *y* axis shows the eigenfrequencies as a function of L-shell. The black lines show the fundamental and third harmonic frequencies, respectively. The exact frequencies and their errors were determined by visual inspection of plots such as Figure 2. Also shown are the Pc3–Pc5 bands defined by Jacobs et al. (1964). Top: Range arrows showing which L-shell range an observation occurred. Each represents conditions where the probability was highest for a given L-shell and OMNI parameter. Blue arrows represent conditions thought to be associated with Kelvin-Helmholtz instability, red arrows for the pressure pulse mechanism, and green arrows for foreshock activity. IMF = interplanetary magnetic field.

Data from the Pello-Muonio station pair (Figure 2) contained data from both the first and third harmonics (based on the arguments in section 3.1). Which harmonic was excited depended on the frequency of the source. Therefore, the ability to say which conditions trigger each harmonic can yield a clue as to which sources were operating at those frequencies.

From table 2, the first harmonic (fundamental) occurred when the solar wind had a higher dynamic pressure/pressure gradient. The solar wind was also dense and fast. The IMF was strongly northward, and there was a high cone angle. Sym H was strongly negative, which suggests that more disturbed conditions were present, similar in some aspects to the observations at the higher latitude.

However, the third harmonic was excited under quieter conditions, when the solar wind had a lower dynamic pressure, though was still fast. The IMF also had a weaker Bz component and a smaller cone angle. These observations are more similar to the lower-latitude pair discussed next.

At lower latitudes, more measurements were made under quieter solar wind conditions when the solar wind was slower and exerted less pressure on the magnetopause. The Sym H index was usually high when measurements were made, indicating a quiet ring current. The IMF was still mostly northward, but its magnitude was weaker. The cone angle was usually small too. Hence, quiet conditions were more conducive for toroidal resonance at plasmaspheric latitudes.

In order to get a better understanding of what the sources were behind these observations, plots of the forms of Figures 2-4 were created for the other seven pairs in Figure 1. These figures have not been shown for brevity, but they allowed for us to see how the observations of high probability varied across the latitude range. The observations were then listed qualitatively for each of the 10 latitudes so that those common to a range of latitudes were easily identifiable. For example, a high probability of detection was seen for low cone angles at all latitudes, whereas a high probability for a disturbed ring current was only seen at high latitudes.

This allowed us to construct the diagram in Figure 5. These qualitative observations were organized by the L-shells at which they occurred. Here, an observation is classified as a condition under which high probability was observed. The range of latitudes under which that observation was seen is illustrated by the double-headed arrows. Figure 5 shows 15 such observations. Below the arrows is a plot showing how the fundamental and third harmonics varied with L-shell. The frequencies and errors of these harmonics were determined visually from Figure 1 and figures such as Figure 2. Hence, these values should not be considered exact but as an approximation for how the eigenfrequencies varied with latitude. Finally, the initials of the station pairs are written along the *x* axis, where the names are given in the caption. The ULF classification boundaries as defined by Jacobs et al. (1964) are also indicated in Figure 5.

The 15 observations have been grouped according to latitude. Observations that were only seen at low latitudes are at the top and those only seen at high latitudes are at the bottom. This grouping allowed us to put observations together that could be related by the source mechanism. Some of the observations were then colored if they were potential signatures of a particular source of ULF waves. A low cone angle and small IMF Bz component suggests that waves were being generated in the foreshock by the ion-cyclotron mechanism. Hence, these two observations have been colored green. Observations that could be associated with the KHI are colored blue and those associated with dynamic pressure pulses are in red. Note that there can be some overlap between this categorization and ultimately, this coloring is a subjective procedure. However, it does allow the reader to pick out key patterns.

Observations labeled as foreshock-related occur across a wider range of latitudes and frequencies and are especially strong at the plasmaspheric latitudes. They also occur when the ring current is quiet. Troitskaya et al. (1971), Takahashi et al. (1984), Le and Russell (1996), Yumoto et al. (1984), and Howard and Menk (2005) all suggest that foreshock activity is the main source of Pc3–Pc4 pulsations. This is defined by the frequency range 6.67–100 mHz, which encompasses the third harmonic of the middle-latitude pair and the fundamental of the lower-latitude pair (and those pairs in between). Hence, this mechanism has the higher-frequency range required to excite the lower-latitude flux tubes.

We can use previous work to understand why the ion-cyclotron mechanism is ineffective at exciting high-latitude flux tubes. Equations (3) and (4) are empirically derived formulae to relate the frequencies generated from the ion-cyclotron mechanism to the IMF magnitude and cone angle (Takahashi et al., 1984; Russell et al., 1983). Both formulae show that the frequency generated is proportional to the IMF magnitude because the proton gyrofrequency depends on it. In order to excite eigenfrequencies in the Pc5 range, the IMF magnitude must be less than 0.87 nT using equation (3), or less than 1.27 nT using equation (4). This calculation assumed a cone angle of 0°. An IMF magnitude this low is unusual so this mechanism is more likely to excite flux tubes at lower latitudes.

$$f_p = 7.6B\cos^2(\theta_c) \tag{3}$$

$$f_p = (0.72 + 4.67\cos(\theta_c))B \tag{4}$$

Foreshock activity also satisfies the observations binned by IMF cone angle. A low cone angle of less than 30° is required for the fast mode waves to couple with magnetospheric flux tubes. Russell et al. (1983) showed that this is because if the cone angle is any greater, then the fast mode waves will not intersect the magnetopause. Instead, they will propagate along the flanks in the magnetosheath. This source also satisfies the MLT distribution of the measurements. Waves generated in the foreshock are expected to couple to flux tubes during daylight hours, which is where the majority of observations occur (Figure 1).

This mechanism operates regardless of how stormy the magnetosphere is, whereas other sources are excited under disturbed conditions. Hence, we see a preference for low cone angles under all storm conditions. The broadband nature of the upstream source also makes it likely. Multiple harmonics are often observed simultaneously (e.g., Engebretson et al., 1986; Wharton et al., 2018) and Takahashi et al. (1984) points out that a broadband source would be needed to explain this. Also, Howard and Menk (2005) suggest that the KHI is not responsible for Pc3/Pc4 harmonics because of the MLT distribution of their events and their associated ellipticity. Our distribution in MLT also supports this.

Figure 6 investigates the ion-cyclotron mechanism further. It displays eigenfrequency-IMF magnitude distributions in the same format as Figures 2-4. However, these data are only for the 9–12 MLT window and only algorithm data taken when the IMF cone angle was less than 30° has been included. This has been accounted for in the probability calculation. On the left is the high-latitude pair, Masi-Sørøya, in the middle is Pello-Muonio, and on the right is the low-latitude pair, Tartu-Nurmijärvi. Note that each data set has its own scale on the probability color bar. The bar charts at the top have the same meaning as in Figures 2-4. Labels showing the interpretation of the harmonic numbers of the bands from section 3.1 have been added to Figure 6.

Plotted over the distributions are the profiles derived from equations (3) and (4) for the upstream-generated frequencies. These formulae have been evaluated for cone angles of 0°, 15°, and 30°, where the thicker line is for 15°. Profiles calculated with equation (4) are shown as solid lines and those calculated with equation (3) are dashed lines. These “source” profiles represent the source frequency as a function of IMF magnitude B. Where these profiles overlap the local eigenfrequency of the station, we should see increased probability because the fast mode waves generated by the source will couple to the local flux tube.

The red bands in Figure 6 are all intersected by the calculated profiles, suggesting that the upstream-generated waves could be responsible for exciting these flux tubes. These red bands cover a wide range of IMF magnitudes though and especially for the higher latitudes, would require low values of the IMF magnitude for excitation ($B < 2$ nT) by this source. This suggests that for the Masi-Sørøya pair that the

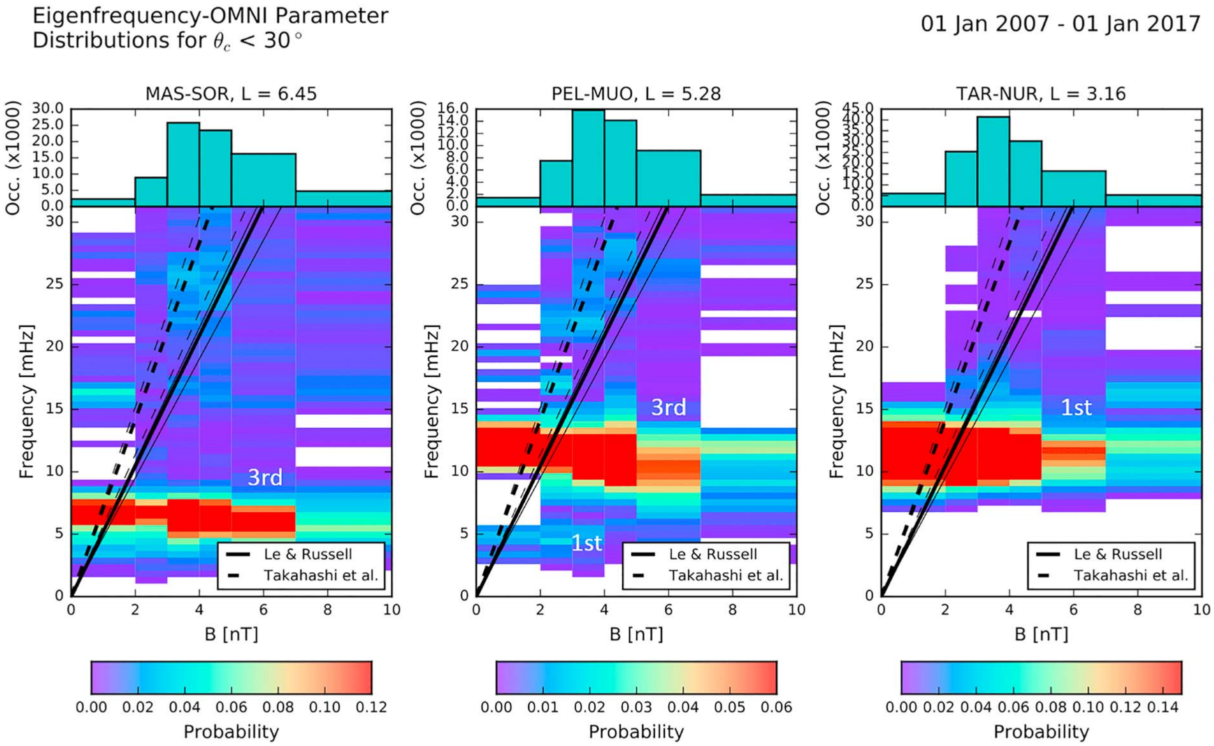

Figure 6. Eigenfrequency-IMF magnitude distributions for cone angles <30° for 9–12 magnetic local time. Left for Masi-Sørøya, middle for Pello-Muonio, and right for Tartu-Nurmijärvi. The heights of the bar charts show the number of data points in IMF magnitude bin. The color in the main subplots show the probability. Solid and dashed lines show the empirical formulae of Le and Russell (1996) and Takahashi et al. (1984). These formulae have been evaluated for cone angles of 15° (thicker line), and 0° and 30° (thinner lines). White labels show the interpretation of the harmonic bands. IMF = interplanetary magnetic field;

ion-cyclotron instability is not the only mechanism operating. At the higher frequencies, there are fainter patches of probability near 25 mHz that lie underneath the source profiles. These eigenfrequencies are far less often observed, but they lie in the Pc3 frequency range and at the right values of B that they could be excited by this source. Even for the low-latitude pair, most of the detections that were made at those frequencies, albeit very few, do lie underneath the source profiles. These data suggest that the ion-cyclotron mechanism can excite the higher harmonics of the flux tubes.

Now we discuss sources related to the magnetopause. Apart from the probability being enhanced during northward IMF, all of the observations related to the KHI or the pressure pulse mechanism correspond to higher latitudes and therefore, lower eigenfrequencies. Two-dimensional MHD simulations by Miura (1987) suggested that the KHI was most likely to excite resonances between 3.2 and 9.3 mHz, and Agapitov et al. (2009) have reported direct observations of MHD waves being driven by magnetopause surface waves. This is the required range to excite the fundamental eigenmode of the Pello-Muonio flux tube and the third harmonic at the higher-latitude pairs. The increase in probability with solar wind speed also supports this mechanism (Figure 2a) and the preference for northward IMF. Masson and Nykyri (2018) and Kavosi and Raeder (2015) state that KHI observations are more common during northward IMF. Other observations of the fundamental mode have found it is most common in the dawn and dusk sectors of the magnetosphere (Anderson et al., 1990; Lessard et al., 1999), suggesting that KHI is the dominant driver. However, Figure 1 shows that the fundamental eigenfrequency is most commonly detected during the daytime, not the dawn or dusk flanks. This could be due to the cross-phase technique being ineffective near the terminator due to weak Hall currents in the unlit ionosphere. The MLT distribution of the measurements varies seasonally due to the different ionospheric conditions (data not shown here). Alternatively, this discrepancy could be due to the frequency width of the driver. It may be that KHI generates power in a very narrow frequency range, and so the cross-phase technique is not sensitive to it. Instead, it only picks out the broadband sources in the solar wind.

The lower frequencies were seen for high-pressure and high spatial pressure gradients in the solar wind (Figure 2d). This suggests that pressure pulses in the solar wind are also a likely driver of the lower-frequency eigenmodes. This is a dayside source that fits the MLT distribution of the measurements. Multiple simulations have shown it is possible to drive a range of flux tubes at their fundamental frequencies with a pressure pulse (Claudepierre et al., 2010; Degeling et al., 2010; Ellington et al., 2016; Elsden & Wright, 2018).

A consistent feature at all latitudes was a preference for detection during periods of northward IMF. Less detections were made during southward IMF, when the nose of the magnetopause was expected to undergo magnetic reconnection. Magnetic reconnection prevents KH waves forming, as the surface of the magnetosphere is continuously removed as open flux (Masson & Nykyri, 2018). However, the pressure pulse mechanism is expected to be independent of IMF direction. It may be the case that during intervals of southward IMF, a pressure pulse enhances magnetic reconnection and transmits energy through this process instead of through fast mode waves propagating into the magnetosphere.

It is worth noting an apparent contradiction with the work of Bentley et al. (2018). They found that waves at 2.5 mHz had more power under southward IMF. However, we have not measured the power spectral density. We only needed sufficient broadband energy to excite a range of flux tubes in order to detect a latitudinal phase difference. It is the occurrence of this process we have measured. Hence, it is entirely possible that there is more power in the flux tubes during southward IMF but it is more likely that the flux tubes are resonating during northward IMF. 2.5 mHz was not necessarily the eigenfrequency at the Gillam magnetometer station they used, so they may not have been detecting standing waves.

FTEs are unlikely to be the required source we need for broadband resonance. We can see this from the lack of observations during southward IMF (Figure 2f) when we would have expected FTEs to be most common. The passage of a sequence of FTEs could potentially generate waves of the right frequency to couple to magnetic flux tubes, but we see no evidence of this process.

It is worth commenting on the differing Sym H relationships at different latitudes. At low latitudes, detections are more likely when the ring current is quiet, whereas at high latitudes, detections are more likely during disturbed intervals. During geomagnetic storms, large and rapid negative excursions of the Sym H values are observed (Gonzalez et al., 1994), and these conditions may be conducive to wave generation (although this is not thought to be a common cause of toroidally polarized waves—see section 1). This is consistent with our discussions about the potential sources of excitation above. The pressure pulse and KHI mechanisms are thought to create lower frequencies and are more likely during disturbed intervals. Therefore, seeing a higher probability of resonance for low Sym H values (more negative) is a reflection of this. Likewise, resonance for the lower latitudes/higher frequencies occurs during quieter times and can be caused by upstream wave generation in the foreshock instead.

The observation that the low-latitude flux tubes are excited predominantly at geomagnetically quiet times could suggest that it is only possible for fast mode waves to penetrate that deep into the magnetosphere when it is quiet. Stormy conditions that disrupt the magnetosphere may prevent the propagation of fast mode waves into the plasmasphere. The plasmapause is also steeper when a storm has occurred (e.g., Kale et al., 2007), which may reflect more of the fast mode energy away, preventing that energy reaching plasmaspheric flux tubes.

4.3. Eigenfrequency Variations

Finally, Table 2 lists some of the key relationships between the eigenfrequency and associated OMNI parameters. Changes in the eigenfrequency indicate that an OMNI parameter may be correlated to changes in either the magnetospheric field strength or plasma mass density. To investigate this, we statistically examined how the most probable eigenfrequency varied with a solar wind parameter, in subplots such as Figure 2a-i for example. We will use this data to describe the procedure, but it is the same for all solar wind variables, MLTs, and latitudes.

First, the eigenfrequency with the greatest probability in each solar wind velocity bin was identified—the most probable eigenfrequency. In the case of Figure 2a-i, this gave eight values, one for each solar wind velocity bin. Then, in each solar wind velocity bin, a spline was fitted to the probabilities of the nine eigenfrequencies centered on the most probable eigenfrequency just identified. This defined a frequency range of 0.832 mHz centered on the most probable eigenfrequency. The spline was used to increase the frequency resolution in this frequency range. A Gaussian curve with three free parameters (location, standard deviation,

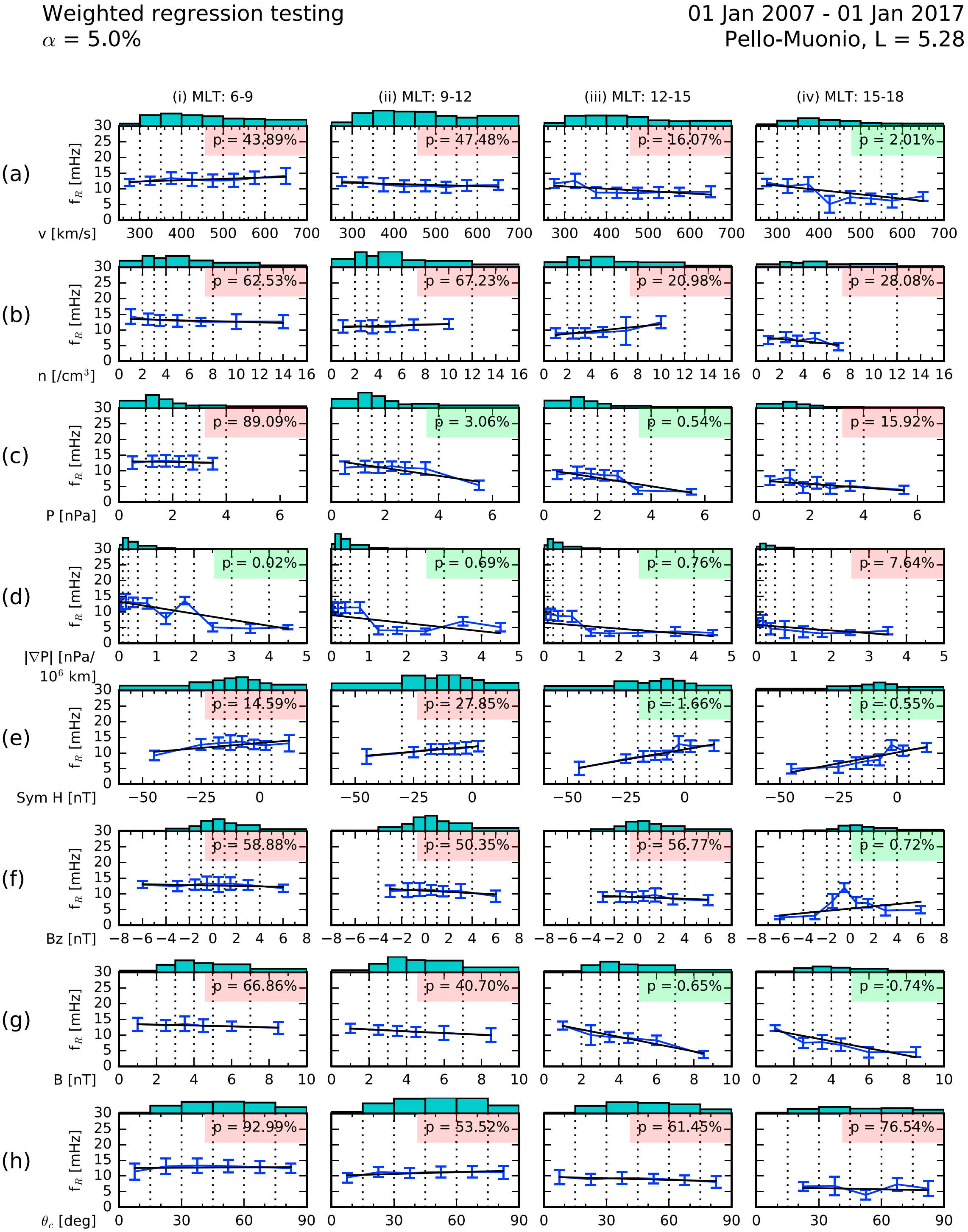

Figure 7. Eigenfrequency variation for eight OMNI parameters using the PEL-MUO station pair. These are the eigenfrequencies where the probability was a maximum. A Gaussian curve has been fitted to the maximum and its eight nearest frequencies to get standard deviation (error bars). Black lines show the line of best fit determined by weighted least squares. (a) Solar wind velocity v, (b) solar wind density n, (c) solar wind dynamic pressure P, (d) modulus of the solar wind dynamic pressure gradient $|\nabla P|$, (e) Sym H index, (f) IMF Bz component B_z, (g) IMF magnitude B, and (h) IMF cone angle θ_c. The four columns, (i) to (iv), represent four magnetic local time bins, which are written at the top. Color in the main plot represents probability (see color bars on the right). The bar plot above each colored plot shows the amount of data in each OMNI parameter column. Labels in the main plot shows the significance of the gradient determined by weighted least squares fitting. It is highlighted green if it is significant (below α) or red if insignificant; α is the significance level. IMF = interplanetary magnetic field;

and amplitude) could then be fitted to the probabilities in this frequency range. The mean f_i and standard deviation σ_i of this curve were used to represent the most probable eigenfrequency and its error. By doing this in each solar wind velocity bin, we could then plot the eigenfrequency as a function of solar wind velocity, and attach an error to the eigenfrequency. This process was repeated for the other MLT sectors and Omni parameters.

This data can be seen in Figure 7a-i as the blue error bars, where the means are joined by a blue line. We have used this to represent the eigenfrequency profile with any given solar wind parameter. Figure 7 shows this procedure applied to all of the subplots from Figure 2. The layout of Figure 7 corresponds to that in Figure 2. The bar plot above each subplot has the exact same meaning as in Figure 2: The height of the bars represents the number of data points in each solar wind parameter bin.

In some cases, the fitting of the Gaussian curve failed. This only happened for a few bins that had a very small quantity of data (e.g., Figure 7d-iv). In these cases, the data point was removed from the analysis. There is also uncertainty due to the harmonic number of the eigenfrequency. For example, if the most probable eigenfrequency in one solar wind bin is the third harmonic, but in the next it is the first harmonic, this will create large jumps in the eigenfrequency profile. To reduce the effect of these, if the determined eigenfrequency differed from both of the eigenfrequencies in the neighboring bins by more than 6 mHz, it was removed. Large jumps could also occur for bins with very little data. This process is limited by the difficulty in determining the harmonic numbers in each bin with certainty. However, from Figure 1, we know that the most probable eigenfrequency for the Pello-Muonio pair corresponded to the third harmonic, so we expect most of the data points to be related to this harmonic.

Next, we fitted a straight line to the eigenfrequency profiles using weighted least squares regression. These formula can be found in Bevington and Robinson (2003). The midpoints of each solar wind parameter bin x_i were used as the x values.

Once we had determined the line of best fit, we performed a t test on the gradient to determine whether there was a significant relationship between the eigenfrequency and an associated solar wind variable. The null hypothesis was that there was no relationship and the alternative hypothesis that there was. The significance level α at which we rejected the null hypothesis was set at 5.0%, which is written at the top left of Figure 7. The t statistic was calculated as the gradient divided by its standard error. The number of degrees of freedom was the number of OMNI parameter bins minus 2, because the gradient and intercept are known. The p value could then be calculated from the Student's t distribution; p represents the probability of obtaining a value of t randomly and if it is less than α, the null hypothesis is rejected and we have found a significant gradient.

For each subplot in Figure 7, the p value is shown in the highlighted box. The box is colored green if $p < \alpha$, and thus, the null hypothesis was rejected. Otherwise, the box is colored red. Only the subplots where $p < \alpha$ are considered to have a significant relationship between the eigenfrequency and the solar wind variable. These significant relationships have been tabulated in Table 2.

Only 11 of the 28 subplots in Figure 7 show a significant relationship. None of the parameters have a significant relationship in every MLT sector. The statistical test has also not identified all of the relationships we might have identified by eye. For example, in Figure 7e-ii, there is a visually clear gradient, but it was not great enough to be significant. The opposite has also occurred. A significant relationship has been identified in Figure 7f-iv, but it is clear from visual inspection that this is not a linear relationship. We now discuss some of these significant relationships, which existed in at least two MLT sectors for a given parameter.

First, the eigenfrequency has been observed to decrease with solar wind dynamic pressure between 9 and 15 MLT. The eigenfrequency also decreases with pressure gradient between 6 and 15 MLT and with IMF magnitude between 12 and 18 MLT. However, the eigenfrequency increases with Sym H index. It could be argued that these relationships hold in other MLT sectors, it is just that they were not significant enough to pass the analysis. All of these relationships suggest that the eigenfrequency at the Pello-Muonio pair decreases during more disturbed conditions. This either implies a weakening of the magnetic field strength or an increase in plasma mass density (or both). This observation agrees with Sandhu, Yeoman, and Rae (2018) and Takahashi et al. (2002), who found that during geomagnetically active conditions, the eigenfrequencies of a given flux tube decreased relative to quiet times. This was attributed to an enhancement in the ring current weakening the magnetic field in the middle magnetosphere (e.g., Ganushkina et al., 2010). The location of the ring current relative to the flux tube under observation will also influence how much the magnetic field is depressed there. Takahashi et al. (2002) also found a correlation between the fundamental eigenfrequency and the sunspot cycle. Investigation of solar cycle variation is left to a future study.

It is thought that the magnetic field has a greater influence over the value of the eigenfrequencies than the plasma mass density (Sandhu, Yeoman, & Rae 2018). It is not entirely clear how changes in geomagnetic activity will affect the plasma mass density. The cold population may experience convective erosion under enhanced solar wind driving, which acts to decrease the mass density with increasing geomagnetic activity (e.g., Dent et al., 2006; Denton et al., 2006; Menk et al., 2014; Sandhu et al., 2017). This would increase the eigenfrequencies. In contrast, higher solar wind coupling can increase the energy and density of the ring current (Sandhu, Rae, et al., 2018). This would enhance the magnetic field of the ring current and weaken the background field, decreasing the eigenfrequencies as observed. Therefore, it is unclear how exactly the total plasma mass density changes in response to increased disturbance, only that the ring current will increase in intensity. We note that the circulation and transport of plasma in the inner magnetosphere plays a role in the range of eigenfrequencies supported. However, further investigation of these complex processes is beyond the scope of this study.

The equivalent statistical analysis for Tartu-Nurmijärvi at low latitudes yielded no significant relationships for any parameter and hence it is not presented. The eigenfrequencies at this station pair, within the plasmasphere, did not change in response to changing solar wind conditions. This may simply be because this flux tube is much deeper within the magnetosphere that the solar wind has less influence on it. During 2007–2017 (the duration of this survey), this pair resided at $L \sim 3.2$, so would have been concealed by the plasmapause nearly all of the time. Only the strongest geomagnetic storms would have been able to shrink the plasmasphere enough to bring this flux tube into the plasmatrough, and these events will barely have featured in the statistical analysis.

For the Masi-Sørøya pair, the equivalent analysis only yielded one signficant relationship out of a possible 28, so is again not represented. The eigenfrequency only significantly decreased with increasing spatial pressure gradient between 6–9 MLT. This relationship also existed for the Pello-Muonio pair and is likely for the same aforementioned reasons. However, it is interesting that at the higher latitudes, where the magnetosphere is expected to undergo more dynamic changes, that there are almost no significant relationships between the eigenfrequency and solar wind variables. A possible solution to this is that the ring current is the dominant factor that can change the eigenfrequencies in the magnetosphere. At these higher and lower latitudes, it may be that the ring current has less influence on these flux tubes. Thus the relationships between the eigenfrequencies and the ring current are weaker at these latitudes.

5. Summary

We applied the cross-phase method to 10 years of IMAGE magnetometer data to determine under what conditions the technique is most effective at measuring the eigenfrequencies of the local magnetic field. This also enabled us to understand under what conditions we see broadband excitation. This is the largest such study of its kind to date.

It was found that the higher eigenfrequencies, approximately in the Pc3 and Pc4 ranges, were preferentially detected under quiet conditions and are most likely excited by waves generated in the foreshock by the ion-cyclotron instability. The lower eigenfrequencies, approximately in the Pc5 range, were preferentially detected when the magnetosphere was undergoing some dynamic change in its structure. The two sources most likely for this excitation are solar wind dynamic pressure pulses and the KHI.

The eigenfrequencies were also observed to decrease with solar wind dynamic pressure, dynamic pressure gradient and IMF magnitude, as well as increasing with Sym H index, at mid-latitudes. In summary, the eigenfrequencies decreased during disturbed times. This occurs because the ring current intensifies during disturbed times and the magnetic field of the ring current increases and depresses the background field. This reduces the local eigenfrequencies. Thus, we think that changes in the magnetic field dominate over changes in the magnetospheric plasma populations. However, these dependencies were not observed within the plasmasphere or at higher latitudes, suggesting these magnetic flux tubes are less influenced by the ring current.

Acknowledgments

We would like to acknowledge some very helpful conversations with T. Elsden, I. J. Rae, and C. Forsyth. S. J. W. was supported by NERC StudentshipNE/L002493/1. T. K. Y. was supported by STFC Grant ST/H002480/1 and NERC Grant NE/K011766/1. M. K. J. was supported by STFC Grant ST/H002480/1. J. K. S. was supported by STFC Grant ST/N000722/1 and NERC Grant NE/P017185/1. The authors would like to thank the IMAGE magnetometer team for providing the data. The data are available at http://space.fmi.fi/image/beta/ website. The OMNI solar wind data are publicly available from the NASA Space Physics Data Facility, Goddard Space Flight Center (http://omniweb.gsfc.nasa.gov/ow.html). This research used the SPECTRE High Performance Computing Facility at the University of Leicester.

References

Agapitov, O., Glassmeier, K.-H., Plaschke, F., Auster, H.-U., Constantinescu, D., Angelopoulos, V., et al. (2009). Surface waves and field line resonances: A THEMIS case study. *Journal of Geophysical Research*, *114*, A00C27. https://doi.org/10.1029/2008JA013553

Anderson, B. J., Engebretson, M. J., Rounds, S. P., Zanetti, L. J., & Potemra, T. A. (1990). A statistical study of Pc 3-5 pulsations observed by the AMPTE/CCE Magnetic Fields Experiment. 1. Occurrence distributions. *Journal of Geophysical Research*, *95*(A7), 10,495–10,523. https://doi.org/10.1029/JA095iA07p10495

Baransky, L., Borovkov, J., Gokhberg, M., Krylov, S., & Troitskaya, V. (1985). High resolution method of direct measurement of the magnetic field lines' eigen frequencies. *Planetary and Space Science*, *33*(12), 1369–1374. https://doi.org/10.1016/0032-0633(85)90112-6

Baransky, L., Belokris, S., Borovkov, Y., Gokhberg, M., Fedorov, E., & Green, C. (1989). Restoration of the meridional structure of geomagnetic pulsation fields from gradient measurements. *Planet Space Sci*, *37*(7), 859–864. https://doi.org/10.1016/0032-0633(89)90136-0

Bentley, S. N., Watt, C. E. J., Owens, M. J., & Rae, I. J. (2018). ULF wave activity in the magnetosphere: Resolving solar wind interdependencies to identify driving mechanisms. *Journal of Geophysical Research: Space Physics*, *123*, 2745–2771. https://doi.org/10.1002/2017JA024740

Berube, D., Moldwin, M. B., & Weygand, J. M. (2003). An automated method for the detection of field line resonance frequencies using ground magnetometer techniques. *Journal of Geophysical Research*, *10*(A9), 1348. https://doi.org/10.1029/2002\protect\LY1\textbraceleftJA\protect\LY1\textbraceright009737

Bevington, P. R., & Robinson, D. K. (2003). *Data reduction and error analysis for the physical sciences* (3rd ed.). California: McGraw-Hill.

Bland, E. C., & McDonald, A. J. (2016). High spatial resolution radar observations of ultralow frequency waves in the southern polar cap. *Journal of Geophysical Research: Space Physics*, *121*, 4005–4016. https://doi.org/10.1002/2015JA022235

Bland, E. C., McDonald, A. J., Menk, F. W., & Devlin, J. C. (2014). Multipoint visualization of ULF oscillations using the Super Dual Auroral Radar Network. *Geophysical Research Letters*, *41*, 6314–6320. https://doi.org/10.1002/2014GL061371

Chappell, C. R., Harris, K. K., & Sharp, G. W. (1971). The dayside of the plasmasphere. *Journal of Geophysical Research*, *76*(31), 7632–7647. https://doi.org/10.1029/JA076i031p07632

Chen, L., & Hasegawa, A. (1974). A theory of long-period magnetic pulsations: 1. Steady state excitation of field line resonance. *Journal of Geophysical Research*, *79*(7), 1024–1032. https://doi.org/10.1029/JA079i007p01024

Chi, P. J., Engebretson, M. J., Moldwin, M. B., Russell, C. T., Mann, I. R., Hairston, M. R., et al. (2013). Sounding of the plasmasphere by Mid-continent MAgnetoseismic Chain (McMAC) magnetometers. *Journal of Geophysical Research: Space Physics*, *118*, 3077–3086. https://doi.org/10.1002/jgra.50274

Chi, P. J., Russell, C. T., Musman, S., Peterson, W. K., Le, G., Angelopoulos, V., et al. (2000). Plasmaspheric depletion and refilling associated with the September 25, 1998 magnetic storm observed by ground magnetometers at L = 2. *Geophysical Research Letters*, *27*(5), 633–636. https://doi.org/10.1029/1999GL010722

Claudepierre, S. G., Hudson, M. K., Lotko, W., Lyon, J. G., & Denton, R. E. (2010). Solar wind driving of magnetospheric ULF waves: Field line resonances driven by dynamic pressure fluctuations. *Journal of Geophysical Research*, *115*, A11202. https://doi.org/10.1029/2010JA015399

Clausen, L. B. N., Yeoman, T. K., Behlke, R., & Lucek, E. A. (2008). Multi-instrument observations of a large scale Pc4 pulsation. *Annals of Geophysics*, *26*(1), 185–199. https://doi.org/10.5194/angeo-26-185-2008

Cummings, W. D., O'Sullivan, R. J., & Coleman, P. J. (1969). Standing Alfvén waves in the magnetosphere. *Journal of Geophysical Research*, *74*(3), 778–793. https://doi.org/10.1029/JA074i003p00778

Degeling, A. W., Rankin, R., Kabin, K., Rae, I. J., & Fenrich, F. R. (2010). Modeling ULF waves in a compressed dipole magnetic field. *Journal of Geophysical Research*, *115*, A10212. https://doi.org/10.1029/2010JA015410

Dent, Z. C., Mann, I. R., Goldstein, J., Menk, F. W., & Ozeke, L. G. (2006). Plasmaspheric depletion, refilling, and plasmapause dynamics: A coordinated ground-based and IMAGE satellite study. *Journal of Geophysical Research*, *111*, A03205. https://doi.org/10.1029/2005JA011046

Denton, R. E., Takahashi, K., Galkin, I. A., Nsumei, P. A., Huang, X., Reinisch, B. W., et al. (2006). Distribution of density along magnetospheric field lines. *Journal of Geophysical Research*, *111*, A04213. https://doi.org/10.1029/2005JA011414

Dungey, J. (1968). Hydromagnetic Waves. In S. Matsushita & W. H. Campbell (Eds.), *Physics of geomagnetic phenomena, chap. 6* (pp. 913–933). New York: Academic Press.

Elkington, S. R., Hudson, M. K., & Chan, A. A. (1999). Acceleration of relativistic electrons via drift-resonant interaction with toroidal-mode Pc-5 ULF oscillations. *Geophysical Research Letters*, *26*(21), 3273–3276. https://doi.org/10.1029/1999GL003659

Ellington, S. M., Moldwin, M. B., &Liemohn, M. W., (2016). Local time asymmetries and toroidal field line resonances: Global magnetospheric modeling in SWMF. *Journal of Geophysical Research: Space Physics*, *121*, 2033–2045. https://doi.org/10.1002/2015JA021920

Elsden, T., & Wright, A. N. (2018). The broadband excitation of 3-D Alfvén resonances in a MHD waveguide. *Journal of Geophysical Research: Space Physics*, *123*, 530–547. https://doi.org/10.1002/2017JA025018

Engebretson, M. J., Zanetti, L. J., Potemra, T. A., & Acuna, M. H. (1986). Harmonically structured ULF pulsations observed by the AMPTE CCE Magnetic Field Experiment. *Geophysical Research Letters*, *13*(9), 905–908. https://doi.org/10.1029/GL013i009p00905

Fenrich, F. R., Samson, J. C., Sofko, G., & Greenwald, R. A. (1995). ULF high- and low-m field line resonances observed with the Super Dual Auroral Radar Network. *Journal of Geophysical Research*, *100*(A11), 21,535–21,547. https://doi.org/10.1029/95JA02024

Ganushkina, N. Y., Liemohn, M. W., Kubyshkina, M. V., Ilie, R., & Singer, H. J. (2010). Distortions of the magnetic field by storm-time current systems in Earth's magnetosphere. *Annals of Geophysics*, *28*(1), 123–140. https://doi.org/10.5194/angeo-28-123-2010

Gonzalez, W. D., Joselyn, J. A., Kamide, Y., Kroehl, H. W., Rostoker, G., Tsurutani, B. T., & Vasyliunas, V. M. (1994). What is a geomagnetic storm? *Journal of Geophysical Research*, *99*(A4), 5771–5792. https://doi.org/10.1029/93JA02867

Hasegawa, A., Tsui, K. H., & Assis, A. S. (1983). A theory of long period magnetic pulsations. 3. Local field line oscillations. *Geophysical Research Letters*, *10*(8), 765–767. https://doi.org/10.1029/GL010i008p00765

Henry, Z. W., Nykyri, K., Moore, T. W., Dimmock, A. P., & Ma, X. (2017). On the dawn-dusk asymmetry of the Kelvin-Helmholtz instability between 2007 and 2013. *Journal of Geophysical Research: Space Physics*, *122*, 11,888–11,900. https://doi.org/10.1002/2017JA024548

Hocke, K. (1998). Phase estimation with the Lomb-Scargle periodogram method. *Annals of Geophysics*, *16*(3), 356–358.

Howard, T. A., & Menk, F. W. (2005). Ground observations of high-latitude Pc3-4 ULF waves. *Journal of Geophysical Research*, *110*, A04205. https://doi.org/10.1029/2004JA010417

Hughes, W. J., & Southwood, D. J. (1976). The screening of micropulsation signals by the atmosphere and ionosphere. *Journal of Geophysical Research*, *81*(19), 3234–3240. https://doi.org/10.1029/JA081i019p03234

Jacobs, J. A., Kato, Y., Matsushita, S., & Troitskaya, V. A. (1964). Classification of geomagnetic micropulsations. *Journal of Geophysical Research*, *69*(1), 180–181. https://doi.org/10.1029/JZ069i001p00180

James, M. K., Yeoman, T. K., Mager, P. N., & Klimushkin, D. Y. (2013). The spatio-temporal characteristics of ULF waves driven by substorm injected particles. *Journal of Geophysical Research: Space Physics*, *118*, 1737–1749. https://doi.org/10.1002/jgra.50131

Kale, Z. C., Mann, I. R., Waters, C. L., Goldstein, J., Menk, F. W., & Ozeke, L. G. (2007). Ground magnetometer observation of a cross-phase reversal at a steep plasmapause. *Journal of Geophysical Research*, *112*, A10222. https://doi.org/10.1029/2007JA012367

Kavosi, S., & Raeder, J. (2015). Ubiquity of Kelvin-Helmholtz waves at Earth's magnetopause. *Nature Communications*, *6*, 7019. https://doi.org/10.1038/ncomms8019

Kawano, H., Yumoto, K., Pilipenko, V. A., Tanaka, Y. M., Takasaki, S., Iizima, M., & Seto, M. (2002). Using two ground stations to identify magnetospheric field line eigenfrequency as a continuous function of ground latitude. *Journal of Geophysical Research*, *107*(A8), 1202. https://doi.org/10.1029/2001JA000274

Kepko, L., Spence, H. E., & Singer, H. J. (2002). ULF waves in the solar wind as direct drivers of magnetospheric pulsations. *Geophysical Research Letters*, *29*(8), 1197. https://doi.org/10.1029/2001GL014405

Lanzerotti, L. J., & Fukunishi, H. (1974). Modes of magnetohydrodynamic waves in the magnetosphere. *Reviews of Geophysics*, *12*(4), 724–729. https://doi.org/10.1029/RG012i004p00724

Le, G., & Russell, C. T. (1996). Solar wind control of upstream wave frequency. *Journal of Geophysical Research*, *101*(A2), 2571–2575. https://doi.org/10.1029/95JA03151

Lessard, M. R., Hudson, M. K., & Lühr H. (1999). A statistical study of Pc3-Pc5 magnetic pulsations observed by the AMPTE/Ion Release Module satellite. *Journal of Geophysical Research*, *104*(A3), 4523–4538. https://doi.org/10.1029/1998JA900116

Lichtenberger, J., Clilverd, M. A., Heilig, B., Vellante, M., Manninen, J., Rodger, C. J., et al. (2013). The plasmasphere during a space weather event: First results from the PLASMON project. *Journal of Space Weather and Space Climate*, *3*, 13. https://doi.org/10.1051/swsc/2013045

Lomb, N. R. (1976). Least-squares frequency analysis of unequally spaced data. *The AAPS Journal*, *39*, 447–462. https://doi.org/10.1007/BF00648343

Luhr, H. (1994). The IMAGE magnetometer network. *STEP International Newsletter*, *4*, 4–6.

Masson, A., & Nykyri, K. (2018). Kelvin-Helmholtz instability: Lessons learned and ways forward. *Space Science Reviews*, *214*(4), 18. https://doi.org/10.1007/s11214-018-0505-6

Mathie, R. A., Menk, F. W., Mann, I. R., & Orr, D. (1999). Discrete field line resonances and the Alfvén continuum in the outer magnetosphere. *Geophysical Research Letters*, *26*(6), 659–662. https://doi.org/10.1029/1999GL900104

Menk, F., Kale, Z., Sciffer, M., Robinson, P., Waters, C., Grew, R., et al. (2014). Remote sensing the plasmasphere, plasmapause, plumes and other features using ground-based magnetometers. *Journal of Space Weather and Space Climate*, *4*(A34), 16. https://doi.org/10.1051/swsc/2014030

Menk, F. W., Mann, I. R., Smith, A. J., Waters, C. L., Clilverd, M. A., & Milling, D. K. (2004). Monitoring the plasmapause using geomagnetic field line resonances. *Journal of Geophysical Research*, *109*, A04216. https://doi.org/10.1029/2003JA010097

Menk, F. W., Orr, D., Clilverd, M. A., Smith, A. J., Waters, C. L., Milling, D. K., & Fraser, B. J. (1999). Monitoring spatial and temporal variations in the dayside plasmasphere using geomagnetic field line resonances. *Journal of Geophysical Research*, *104*(A9), 19,955–19,969. https://doi.org/10.1029/1999JA900205

Milan, S. E., Gosling, J. S., & Hubert, B. (2012). Relationship between interplanetary parameters and the magnetopause reconnection rate quantified from observations of the expanding polar cap. *Journal of Geophysical Research*, *117*, A03226. https://doi.org/10.1029/2011JA017082

Milling, D. K., Mann, I. R., & Menk, F. W. (2001). Diagnosing the plasmapause with a network of closely spaced ground-based magnetometers. *Geophysical Research Letters*, *28*(1), 115–118. https://doi.org/10.1029/2000GL011935

Miura, A. (1987). Simulation of Kelvin-Helmholtz instability at the magnetospheric boundary. *Journal of Geophysical Research*, *92*(A4), 3195–3206. https://doi.org/10.1029/JA092iA04p03195

Motoba, T., Ebihara, Y., Ogawa, Y., Kadokura, A., Engebretson, M. J., Angelopoulos, V., et al. (2018). On the driver of daytime Pc3 auroral pulsations. *Geophysical Research Letters*, *46*, 553–561. https://doi.org/10.1029/2018GL080842

Neugebauer, M., & Snyder, C. W. (1966). Mariner 2 observations of the solar wind: 1. Average properties. *Journal of Geophysical Research*, *71*(19), 4469–4484. https://doi.org/10.1029/JZ071i019p04469

O'Brien, T. P., & Moldwin, M. B. (2003). Empirical plasmapause models from magnetic indices. *Geophysical Research Letters*, *30*(4), 1152. https://doi.org/10.1029/2002GL016007

Obana, Y., Menk, F. W., Sciffer, M. D., & Waters, C. L. (2008). Quarter-wave modes of standing Alfvén waves detected by cross-phase analysis. *Journal of Geophysical Research*, *113*, A08203. https://doi.org/10.1029/2007JA012917

Orr, D., & Hanson, H. (1981). Geomagnetic pulsation phase patterns over an extended latitudinal array. *Journal of Atmospheric and Terrestrial Physics*, *43*(9), 899–910. https://doi.org/10.1016/0021-9169(81)90081-7

Orr, D., & Matthew, J. A. (1971). The variation of geomagnetic micropulsation periods with latitude and the plasmapause. *Planetary and Space Science*, *19*(8), 897–905. https://doi.org/10.1016/0032-0633(71)90141-3

Poulter, E., Allan, W., Keys, J., & Nielsen, E. (1984). Plasmatrough ion mass densities determined from ULF pulsation eigenperiods. *Planetary and Space Science*, *32*(9), 1069–1078. https://doi.org/10.1016/0032-0633(84)90132-6

Pu, Z.-Y., & Kivelson, M. G. (1983). Kelvin-Helmholtz Instability at the magnetopause: Solution for compressible plasmas. *Journal of Geophysical Research*, *88*(A2), 841–852. https://doi.org/10.1029/JA088iA02p00841

Rae, I. J., Watt, C. E. J., Fenrich, F. R., Mann, I. R., Ozeke, L. G., & Kale, A. (2007). Energy deposition in the ionosphere through a global field line resonance. *Annals of Geophysics*, *25*(12), 2529–2539. https://doi.org/10.5194/angeo-25-2529-2007

Russell, C. T., & Elphic, R. C. (1979). ISEE observations of flux transfer events at the dayside magnetopause. *Geophysical Research Letters*, *6*(1), 33–36. https://doi.org/10.1029/GL006i001p00033

Russell, C. T., Luhmann, J. G., Odera, T. J., & Stuart, W. F. (1983). The rate of occurrence of dayside Pc 3,4 pulsations: The L-value dependence of the IMF cone angle effect. *Geophysical Research Letters*, *10*(8), 663–666. https://doi.org/10.1029/GL010i008p00663

Samson, J. C., Jacobs, J. A., & Rostoker, G. (1971). Latitude-dependent characteristics of long-period geomagnetic pulsations. *Journal of Geophysical Research*, *76*(16), 3675–3683. https://doi.org/10.1029/JA076i016p03675

Sandhu, J. K., Rae, I. J., Freeman, M. P., Forsyth, C., Gkioulidou, M., Reeves, G. D., et al. (2018). Energization of the Ring Current by Substorms. *Journal of Geophysical Research: Space Physics*, *123*, 8131–8148. https://doi.org/10.1029/2018JA025766

Sandhu, J. K., Yeoman, T. K., Fear, R. C., & Dandouras, I. (2016a). A statistical study of magnetospheric ion composition along the geomagnetic field using the Cluster spacecraft for L values between 5.9 and 9.5. *Journal of Geophysical Research: Space Physics*, *121*, 2194–2208. https://doi.org/10.1002/2015JA022261

Sandhu, J. K., Yeoman, T. K., Fear, R. C., & Dandouras, I. (2016b). A statistical study of magnetospheric electron density using the Cluster spacecraft. *Journal of Geophysical Research: Space Physics*, *121*, 11,042–11,062. https://doi.org/10.1002/2016JA023397

Sandhu, J. K., Yeoman, T. K., James, M. K., Rae, I. J., & Fear, R. C. (2018). Variations of high-latitude geomagnetic pulsation frequencies: A comparison of time-of-flight estimates and IMAGE magnetometer observations. *Journal of Geophysical Research: Space Physics*, *123*, 567–586. https://doi.org/10.1002/2017JA024434

Sandhu, J. K., Yeoman, T. K., Rae, I. J., Fear, R. C., & Dandouras, I. (2017). The dependence of magnetospheric plasma mass loading on geomagnetic activity using Cluster. *Journal of Geophysical Research: Space Physics*, *122*, 9371–9395. https://doi.org/10.1002/2017JA024171

Sandhu, J. K., Yeoman, T. K., & Rae, I. J. (2018). Variations of field line eigenfrequencies with ring current intensity. *Journal of Geophysical Research: Space Physics*, *123*, 9325–9339. https://doi.org/10.1029/2018JA025751

Scargle, J. D. (1982). Studies in astronomical time series analysis. II—Statistical aspects of spectral analysis of unevenly spaced data. *Astronomy Journal*, *263*, 835–853. https://doi.org/10.1086/160554

Shen, X.-C., Shi, Q., Wang, B., Zhang, H., Hudson, M. K., Nishimura, Y., et al. (2018). Dayside Magnetospheric and Ionospheric Responses to a Foreshock Transient on 25 June 2008: 1. FLR Observed by Satellite and Ground-Based Magnetometers. *Journal of Geophysical Research: Space Physics*, *123*, 6335–6346. https://doi.org/10.1029/2018JA025349

Shi, X., Ruohoniemi, J. M., Baker, J. B. H., Lin, D., Bland, E. C., Hartinger, M. D., & Scales, W. A. (2018). Survey of ionospheric Pc3-5 ULF wave signatures in SuperDARN high time resolution data. *Journal of Geophysical Research: Space Physics*, *123*, 4215–4231. https://doi.org/10.1029/2017JA025033

Southwood, D. (1974). Some features of field line resonances in the magnetosphere. *Planetary and Space Science*, *22*(3), 483–491. https://doi.org/10.1016/0032-0633(74)90078-6

Sugiura, M., & Wilson, C. R. (1964). Oscillation of the geomagnetic field lines and associated magnetic perturbations at conjugate points. *Journal of Geophysical Research*, *69*(7), 1211–1216. https://doi.org/10.1029/JZ069i007p01211

Takahashi, K., & Denton, R. E. (2007). Magnetospheric seismology using multiharmonic toroidal waves observed at geosynchronous orbit. *Journal of Geophysical Research*, *112*, A05204. https://doi.org/10.1029/2006JA011709

Takahashi, K., Denton, R. E., & Gallagher, D. (2002). Toroidal wave frequency at L = 6-10: Active Magnetospheric Particle Tracer Explorers/CCE observations and comparison with theoretical model. *Journal of Geophysical Research*, *107*(A2), 1020. https://doi.org/10.1029/2001JA000197

Takahashi, K., Denton, R. E., & Singer, H. J. (2010). Solar cycle variation of geosynchronous plasma mass density derived from the frequency of standing Alfvén waves. *Journal of Geophysical Research*, *115*, A07207. https://doi.org/10.1029/2009JA015243

Takahashi, K., Lee, D., Merkin, V. G., Lyon, J. G., & Hartinger, M. D. (2016). On the origin of the dawn-dusk asymmetry of toroidal Pc5 waves. *Journal of Geophysical Research: Space Physics*, *121*, 9632–9650. https://doi.org/10.1002/2016JA023009

Takahashi, K., & McPherron, R. L. (1982). Harmonic structure of Pc 3-4 pulsations. *Journal of Geophysical Research*, *87*(A3), 1504–1516. https://doi.org/10.1029/JA087iA03p01504

Takahashi, K., & McPherron, R. L. (1984). Standing hydromagnetic oscillations in the magnetosphere. *Planetary and Space Science*, *32*(11), 1343–1359. https://doi.org/10.1016/0032-0633(84)90078-3

Takahashi, K., McPherron, R. L., & Terasawa, T. (1984). Dependence of the spectrum of Pc 3-4 pulsations on the interplanetary magnetic field. *Journal of Geophysical Research*, *89*(A5), 2770–2780. https://doi.org/10.1029/JA089iA05p02770

Troitskaya, V., Tlyasova-Bakunina, T., & Guglielmi, A. V. (1971). The connection of Pc2-4 pulsations with interplanetary magnetic field. *Dolk. Akad. Nauk SSSR*, *197*(6), 1312–1314.

Walker, A., Greenwald, R., Stuart, W., & Green, C. (1979). Stare auroral radar observations of Pc 5 geomagnetic pulsations. *Journal of Geophysical Research*, *84*(A7), 3373–3388. https://doi.org/10.1029/JA084iA07p03373

Warner, M., & Orr, D. (1979). Time of flight calculations for high latitude geomagnetic pulsations. *Planetary and Space Science*, *27*(5), 679–689. https://doi.org/10.1016/0032-0633(79)90165-X

Waters, C. L., Menk, F. W., & Fraser, B. J. (1991). The resonance structure of low latitude Pc3 geomagnetic pulsations. *Geophysical Research Letters*, *18*(12), 2293–2296. https://doi.org/10.1029/91GL02550

Waters, C. L., Menk, F. W., & Fraser, B. J. (1994). Low latitude geomagnetic field line resonance: Experiment and modeling. *Journal of Geophysical Research*, *99*, 17,547–17,558. https://doi.org/10.1029/94JA00252

Waters, C. L., Samson, J. C., & Donovan, E. F. (1995). The temporal variation of the frequency of high latitude field line resonances. *Journal of Geophysical Research*, *100*, 7987–7996. https://doi.org/10.1029/94JA02712

Waters, C. L., Samson, J. C., & Donovan E. F. (1996). Variation of plasmatrough density derived from magnetospheric field line resonances. *Journal of Geophysical Research*, *101*(A11), 24,737–24,745. https://doi.org/10.1029/96JA01083

Wharton, S. J., Wright, D. M., Yeoman, T. K., James, M. K., & Sandhu, J. K. (2018). Cross-phase determination of ULF wave harmonic frequencies and their associated plasma mass density distributions. *Journal of Geophysical Research: Space Physics*, *123*, 6231–6250. https://doi.org/10.1029/2018JA025487

Wharton, S. J., Wright, D. M., Yeoman, T. K., & Reimer, A. S. (2019). Identifying ULF wave eigenfrequencies in SuperDARN backscatter using a Lomb-Scargle Cross-phase analysis. *Journal of Geophysical Research: Space Physics*, *124*, 996–1012. https://doi.org/10.1029/2018JA025859

Wright, A. N., & Elsden, T. (2016). The theoretical foundation of 3D Alfvén resonances: Normal modes. *Astronomy Journal*, *833*(2), 230.

Wright, A. N., Elsden, T., & Takahashi, K. (2018). Modeling the dawn/dusk asymmetry of field line resonances. *Journal of Geophysical Research: Space Physics*, *123*, 6443–6456. https://doi.org/10.1029/2018JA025638

Wright, D. M., & Yeoman T. K. (1999). Letter to the editor CUTLASS observations of a high-m ULF wave and its consequences for the DOPE HF Doppler sounder. *Annals of Geophysics*, *17*(11), 1493–1497. https://doi.org/10.1007/s00585-999-1493-3

Yeoman, T. K., Klimushkin, D. Y., & Mager, P. N. (2010). Intermediate-m ULF waves generated by substorm injection: A case study. *Annals of Geophysics*, *28*(8), 1499–1509. https://doi.org/10.5194/angeo-28-1499-2010

Yumoto, K., Saito, T., Tsurutani, B. T., Smith, E. J., & Akasofu, S.-I. (1984). Relationship between the IMF magnitude and Pc 3 magnetic pulsations in the magnetosphere. *Journal of Geophysical Research*, *89*(A11), 9731–9740. https://doi.org/10.1029/JA089iA11p09731